CanmetMATERIALS

Comparison of Fracture Toughness between Large and Small CCTS from Zr-2.5Nb Pressure Tube Material

GCDOCS Workflow ID 34694464

Submitted to the Canadian Nuclear Safety Commission

By

Bruce W. Williams, William R. Tyson, and C. Hari M. Simha

December 2018

DISCLAIMER

Natural Resources Canada makes no representations or warranties respecting the contents of this report, either expressed or implied, arising by law or otherwise, including but not limited to implied warranties or conditions of merchantability or fitness for a particular purpose.

CanmetMATERIALS

GCDOCS Workflow ID 34694464

Comparison of Fracture Toughness between Large and Small CCTS from Zr-2.5Nb Pressure Tube Material

By

Bruce W. Williams, William R. Tyson, and C. Hari M. Simha

SUMMARY

It has been established that fracture toughness measurements of Zr-2.5Nb pressure tube material obtained from Curved Compact Tension Specimens (CCTS) with a width of 17 mm typically provide values lower than corresponding fracture toughness measurements from burst tests. The objective of the current work was to analyse alternative fracture toughness test geometries and assess whether the J-resistance curves might be more representative of the response obtained from rising pressure burst tests with have larger crack extension that typical small-scale specimens. Three test geometries referred to as W17, W34-Small-Pin-Spacing (SPS) and W34-Large-Pin-Spacing (LPS) were considered in the current work. The pin spacing of the W34-SPS specimen was 10 mm compared to a pin spacing of 18.7 mm for the W34-LPS geometry. It has previously been shown that higher forces were required to propagate cracks in the W34-SPS CCTS geometry compared to the W17 CCTS geometry, which could lead to higher fracture toughness values more representative of those obtained from burst tests. In the current work, CCTS tests were carried out on specimens machined from an unirradiated Zr-2.5Nb pressure tube with a thickness of 4.4 mm. Crack tunnelling was observed during CCTS testing of the unirradiated Zr-2.5Nb pressure tube material at room temperature. Extensive finite element analyses conducted in the work demonstrated that out-of-plane loading for the curved specimens and crack tunnelling, which are not accounted for in the ASTM E1820 Standard, did not significantly affect the estimated J-integral of the material. Experiments produced consistent J-R curves for each of the W17, W34-SPS, and W34-LPS CCTS geometries. The stress intensity factor at maximum load was calculated to be 206 and 289 MPa√m for the W17 and W34-SPS CCTS, respectively. Additionally, the crack extension at maximum loads was 140% greater for the W34-SPS CCTS than for the W17 CCTS. The results presented here suggest that the larger CCTS with a small pin-to-pin spacing is a promising alternative to the smaller geometry. More specifically, the larger CCTS allowed J-R curves to be measured to greater crack extensions, more representative of extensions obtained in pressure tube section burst tests. It is realized that the fracture toughness measured at room temperature for unirradiated Zr-2.5Nb CCTS is larger than the upper shelf lower bound fracture toughness limit of 72 MPa√m in the CSA Standards, but the fracture toughness of irradiated, hydrided material will be lower than the room temperature as-received fracture toughness. Hydrided pressure tube material was not considered in the current work due to a potential source of variability but could be considered in future work.

LIST OF ABBREVIATIONS

ASTM	American Society for Testing and Materials
CANDU	CANada Deuterium Uranium
CCL	Critical Crack Length
CCTS	Curved Compact Tension Specimen
CMAT	CanmetMATERIALS
CNSC	Canadian Nuclear Safety Commission
CSA	Canadian Standards Association
C(T)	Compact Tension
DCPD	Direct Current Potential Drop
FEA	Finite Element Analysis
H_{eq}	Hydrogen Equivalent Concentration
LVDT	Linear Variable Differential Transducer
Nb	Niobium
PD	Potential Drop
PT	Pressure Tube
RT	Room Temperature
Zr	Zirconium

LIST OF SYMBOLS

J_{Ic}	Value of J-integral at onset of crack growth
J_e	Elastic component of J integral
J_{pl}	Plastic component of J integral
K_{Ic}	Critical stress-intensity factor at onset of crack growth
ε_o	Strain at onset of yield
ε_p	Effective plastic strain
$\bar{\sigma}$	Effective stress
σ_y	Yield strength
B	Specimen thickness
E	Elastic Modulus
J	J-integral
$J - R$	J-resistance (curve of J-integral vs. crack growth)
K	Stress intensity factor
P	Load
W	Specimen width
a	Crack length
b	Length of remaining ligament
f	Function for C(T) specimen
k	Hardening coefficient
n	Hardening exponent
α	Coefficient in hardening model
γ	Factor in ASTM analysis
η	Factor in ASTM analysis
ν	Poisson's ratio

TABLE OF CONTENTS

Page

CanmetMATERIALS ——————————————————————

1   INTRODUCTION

It is of importance to calculate an accurate Critical Crack Length (CCL) of Zr-2.5Nb pressure tubes, the main pressure boundary used in CANDU reactors. A measure of the fracture toughness may be obtained by a rising pressure burst test performed on ex-service, irradiated Zr-2.5Nb pressure tubes [1]. Fracture toughness measurements are also obtained using Curved Compact Tension Specimens (CCTS). The specimen used by the industry has a width of 17 mm, as described in [2],[3]. As detailed in [1], there are differences in the J-resistance curves between burst tests and 17 mm CCTS. In general, it has been shown that the 17 mm CCTS provide fracture toughness measurements below those of corresponding measurements from burst tests. The amount by which the fracture toughness values measured using the CCTS were lower than the toughness measured using burst tests depended on the ductility of the material (which can be dependent on temperature and chemical composition). For instance, it was shown that the difference between the fracture toughness values was much less for a low-toughness pressure tube than the difference for an intermediate-toughness pressure tube. It was concluded that crack-tip constraint effects could explain the difference in fracture toughness measurements. Consequently, using fracture toughness data from 17 mm wide CCTS may lead to low (conservative) estimates of CCL. The objectives of the current work are to: 1) assess the applicability of the ASTM E1820 [4] procedure for obtaining resistance curves using the CCTS geometry and 2) analyse alternative fracture toughness test geometries and assess whether the crack growth resistance curves might be more representative of the response from rising pressure burst tests.

1.1 Overview of the Report

Section 2 of the report provide details on various geometries, including flat and curved specimens, that can be used to assess the fracture toughness of materials. A review of the alternative geometries relative to the 17 mm width CCTS is presented, but the report focuses on three curved geometries referred to as W17 (the standard 17 mm width geometry), W34-Small-Pin-Spacing (SPS), and W34-Large-Pin-Spacing (LPS) CCTS. The applicability of the ASTM J-integral estimating scheme for curved geometry and crack tunnelling is addressed through finite element (FE) analyses, as detailed in Section 3. The J-integral is used in the current work to quantify resistance to crack growth and the J-values predicted from simulation are compared to corresponding J-values calculated from ASTM procedures. Simulation results are presented for both stationary and growing cracks. Appendix A gives a brief introduction of the J-integral. Additional discussion of the applicability of the ASTM Standard to CCTS is given in Appendix B.

Section 4 details the experimental procedure used in fracture toughness testing of CCTS taken from unirradiated Zr-2.5Nb pressure tube material. Section 5 presents the results of the fracture toughness testing for W17, W34-SPS, and W34-LPS CCTS geometries. This includes presentation of the J-R curves that compare the measured crack growth resistance between the three geometries. The discussion includes details about which specimen geometry would be expected to provide measurements of fracture toughness representative of those from a rising pressure burst test.

CanmetMATERIALS

2   FRACTURE TOUGHNESS TEST GEOMETRIES

Figure 1 displays the C(T) specimen geometry for J-integral testing equivalent to that recommended in the ASTM standard E1820 [4] (hereafter the Standard). For materials that do not exhibit ductility, the fracture toughness at crack initiation, K_{IC}, for linear elastic behavior is sought. A modified geometry is permitted as indicated in the notes in the figure. The figure is parametrized in terms of the width W of the sample; other geometrical features of the specimen relevant to analysis are also labelled.
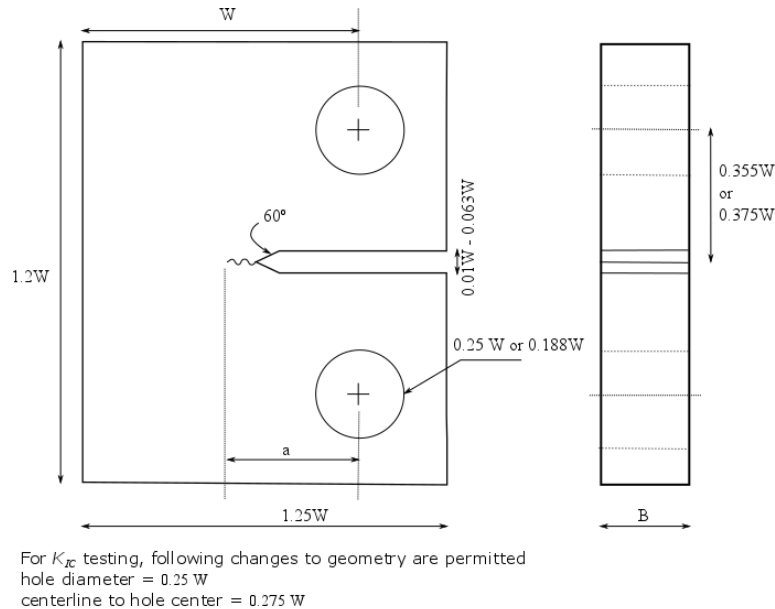

Figure 1: Dimensions for a standard C(T) specimen from the E1820-15 ASTM Standard (2015); adapted from Fig. A2.1 in the Standard

The 17 mm width curved specimen geometry detailed by Chow & Simpson [3] is shown in Figure 2. The geometry of the 17 mm width CCTS conforms to most of the specifications in Annex A2 of the Standard. Specimens tested by Chow and Simpson [3] had width-to-thickness (W/B) ratios ranging between 4.1 and 3.4, and these conform to the W/B range of 2 to 4 specified by the Standard with a modest violation of the upper bound. More significantly, the Standard does not provide advice on testing of curved specimens. The following other departures from the geometry recommended by ASTM are identified:

1. The notch width is 1.5 mm, which is $0.088W$, and is larger than the maximum recommended value of $0.063W = 1.071$ mm.
2. The specimen has out-of-plane curvature on account of it being machined from a tube of diameter 103 mm. Annex A2 of E1820 does not permit curvature.
3. Height of the loading hole from specimen centerline is 4.68 mm which is $0.275W$; this is recommended for K_{IC} testing but not for J-integral testing.
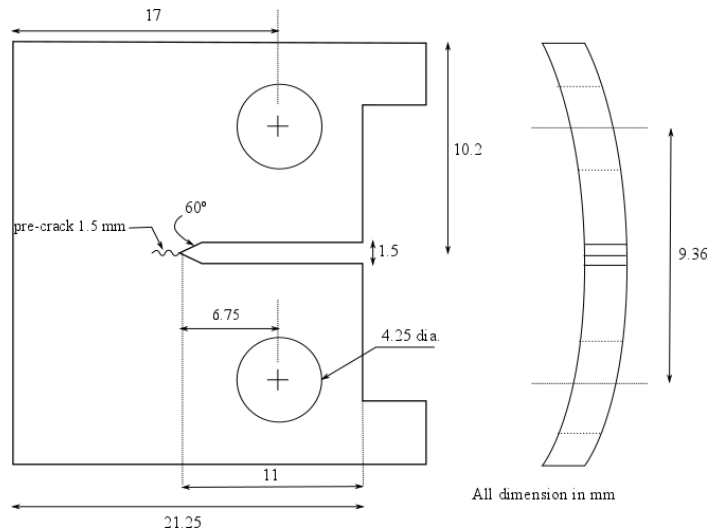
Figure 2: Schematic of Curved Compact Tension Specimen (CCTS); adapted from Fig. 3 of the article by Chow & Simpson [3]; all dimensions in mm.

The CCTS specimen geometry is then a hybrid of what is recommended for K_{IC} testing and J-integral evaluation with the most significant deviation being in the specimen curvature. Chow & Simpson [3],[5] carried out experiments on both flat and curved specimens and compared the J-integrals, evaluated using a combination of procedures from ASTM E399-83 and the article by Ernst et al. [6]. They found no significant difference. Note here, that although ASTM E399-83 has been superseded by the current ASTM E1820, there are no appreciable changes to the analysis procedures for K_{IC} and resistance curve testing, particularly with regards to C(T) specimens. Using plate-theory-based assessment, it was deemed reasonable that the curvature of the sample does not affect the J-integral [3]. It is not clear if the departures of the CCTS geometry from the ASTM recommendations permit the use of ASTM E1820 procedures for evaluating the specimen records and calculating J-integrals. In the next section of this report, finite element (FE) computations are used to address this issue.

2.1 CCTS Geometries: W17, W34-SPS, and W34-LPS

The 17 mm width, or W17, CCTS with a pin spacing of 9.4 mm is shown in Figure 3a. The compact tension specimen with a width of 34 mm and a pin spacing of 18.7 mm, as shown in Figure 3b, is based on the K_{IC} test geometry detailed in ASTM E1820. In the current work, this specimen is referred to as W34-Large-Pin-Spacing (LPS). The W34-modified specimen with a pin spacing of 10 mm studied by Davies, Shewfelt, and Jarvine [7] is shown in Figure 3c. This specimen is referred to as W34-Small-Pin-Spacing (SPS) in the current report. As discussed in [7], based on a limited number of tests on unirradiated Zr-2.5Nb pressure tube material, the J-R curves from burst tests were significantly higher than J-R curves from W17 CCTS. However the J-R curves from burst were similar (only slightly lower) than J-R curves from W34-SPS CCTS. This indicated that the W34-SPS CCTS with the reduced pin spacing could yield fracture toughness measurements more representative of burst tests, compared to the W34-LPS specimen. Fractography was also carried out. Fracture surfaces had a central flat region and narrow shear lips at the surface. Similarity of appearance with fracture surfaces observed in burst

CanmetMATERIALS ——————————————————————————————————

tests was noted. It was also emphasized that the crack extension and fracture in the larger bend-type C(T) specimens approaches the crack extension in burst tests more than smaller specimens.
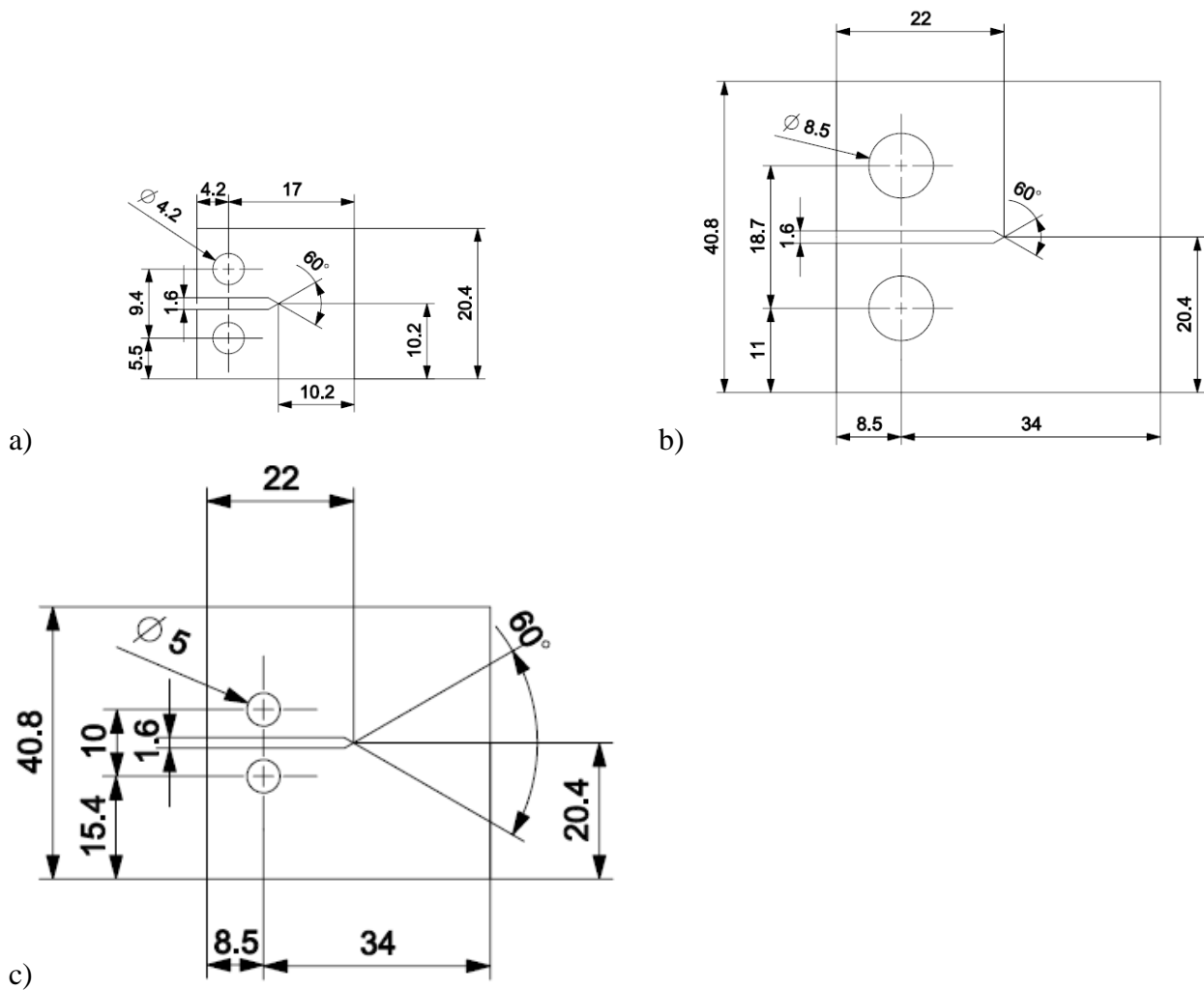

a)

b)

c)

Figure 3: Curved Compact Tension Specimens a) W17, b) W34-LPS, and c) W34-SPS; dimensions in mm.

For W34-SPS and W34-LPS CCTS the value of *W/B* is 8.1 for a 4.2 mm thick specimen, which does not conform to the recommendation of Annex A (section A2.1) of ASTM E1820. For the W34-SPS geometry, the separation of the centerline of the loading holes is 10 mm, which also does not conform to any of the ASTM recommendations. However, the loading hole separation for W34-SPS (10 mm) is approximately the same as for the W17 CCTS (9.4 mm).

2.2 Review of Alternative Test Geometries

Other techniques used to characterize pressure boundary material using small-scale samples, with emphasis on those used for nuclear applications, are presented in this section. Full-scale tests using tube specimens are not addressed here.

2.2.1 Curved Bending Test

Honda [8] developed a novel test to characterize curved un-irradiated specimens of Zr-2.5Nb cut from 4.3 mm thick, 117.8 mm diameter tubes. Some of the specimens were hydrided while under bend loading in some tests to examine the effect of the load on hydride orientation. Burst tests were also performed on tubes with through-wall axial cracks. Instrumentation used in either the bend or the burst specimens was not given in the article. Specimen geometry and load application are shown in Figure 4 where the edges were fixed by being bolted to a fixture.
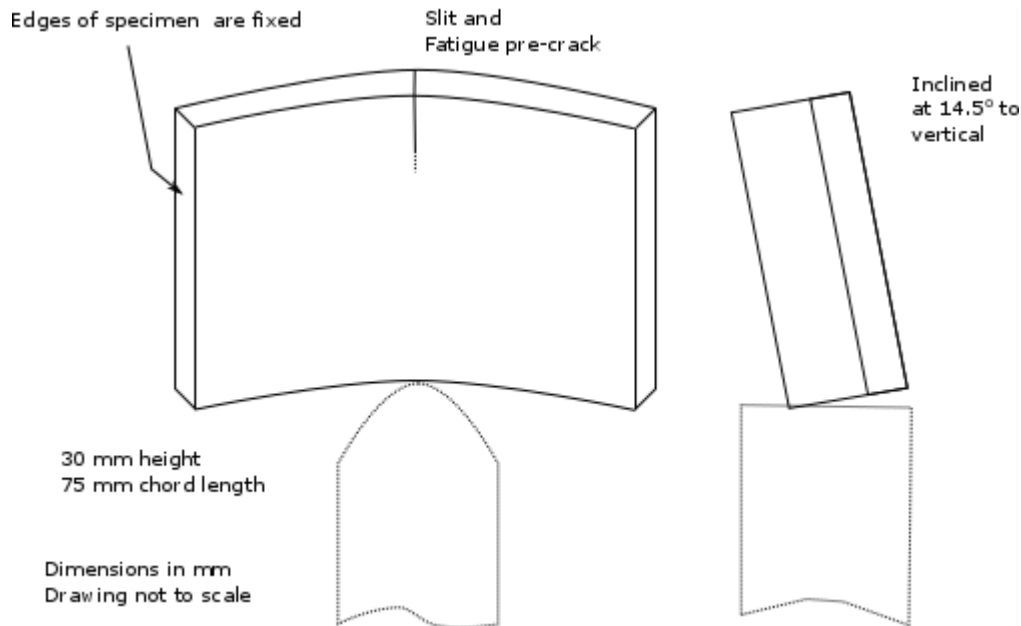
Figure 4: Curved Bend Specimen geometry [8]

The choice of the inclination angle is not discussed in the article. Presumably it was selected to replicate the stress condition in a through-wall crack of the pressure tube. Equations from Newman [9] were modified and used to compute stress-intensity factors for the specimen and the tubes. It was concluded that averages of the stress-intensity factors from the bending and burst specimens were in good agreement. Hydrogen content for this study ranged between 100 ppm and 250 ppm (averages), and temperatures ranged from RT to 300 °C. Though promising, the key disadvantage of this test is that it is not based on a standard and requires specialized equipment.

CanmetMATERIALS

2.2.2 Centre-Cracked Curved Specimen

Wallace [10] developed a center-cracked curved specimen as part of thesis work, and subsequently the geometry was used in experiments carried out by Davies et al. [7]. The specimen geometry is shown in Figure 5. Specimens were machined from CANDU reactor pressure tube material and tested in un-irradiated and un-hydrided conditions at room temperature. Specially designed grips (position of pivot and grip curvature) ensured that the stresses at the crack tip closely matched the stresses at the tip of a through-wall crack in a pressure tube. For comparison purposes, flat, centre-cracked specimens were also tested.
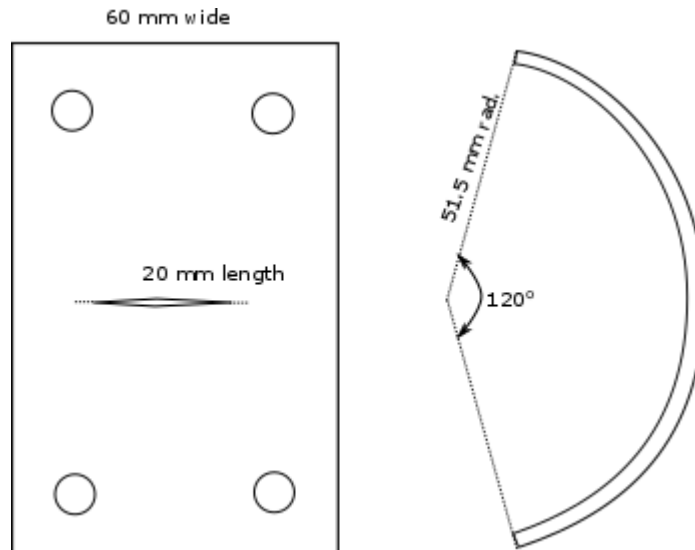

Figure 5: Centre-cracked curved specimen

The specimen had a through-wall crack that was 20-mm long in the axial direction with a 5-mm long fatigue precrack. The potential drop technique was used to monitor crack extension. Resistance curves were obtained using the procedures presented by McCabe & Ernst [11]. Post-test metallographic examination showed significant blunting at the crack tip with a wide primary stretch zone (~2 mm). The primary stretch zone was at an angle of 30° to the original crack plane.

Davies et al. [7] found that, in general, at all crack extensions, the center-cracked specimen yielded toughness values significantly higher than those obtained from burst testing of through-wall-cracked pressure tubes with the crack oriented in the axial direction. Echoing the results of Landes et al. [12], who had tested center-cracked, flat, steel specimens, Davies et al. [7] concluded that center-cracked specimens produced higher resistance curves than C(T) specimens. Indeed, owing to the formation of diverging slip lines in front of the crack tip, it is likely that J-controlled crack tip conditions do not prevail.

Supporting metallographic examination showed low densities of fissures in the primary stretch zone. In contrast, tearing dimples and secondary regions of stretching indicated that the level of triaxiality in the center-cracked specimen was much lower than that in the burst test. A key conclusion was that the crack tips of bend-type C(T) specimens better replicated the triaxiality of the pressure tube burst tests than the centre-cracked specimens.

CanmetMATERIALS

2.2.3 Miniature Compact Tension Specimens

Lucon et al. [13] tested miniature compact tension specimens with $a = 2.7$ mm, $B = 4.14$ mm and $W = 8.3$ mm. The separation between the loading holes was 4.4 mm. This specimen had $W/B = 2$, which conforms to the recommendation of Annex A (section A2.1) of ASTM E1820. The separation between the centrelines of the loading holes conforms to the recommendation of $0.55W$, which is recommended for the K_{Ic} test specimen geometry (see Fig. A2.2 of E1820). For comparison, "full-size" CT specimens with $B = 25$ mm were also tested. All specimens were side grooved to 80% of thickness after fatigue precracking.

In the referenced study, the specimens were fabricated from three reactor pressure vessel steels and a low-alloy steel. Clip gauges were used to measure the crack-mouth opening displacement. Analysis procedures from ASTM E1820-01 and the ISO 12135:2002 Standards were used to obtain resistance curves. There was only a marginal difference between the resistance curves obtained using the two procedures. However, there was a significant difference between the resistance curves obtained for miniature and standard geometries, with the smaller specimens yielding lower curves. It was suggested that the lower fracture toughness and resistance to ductile crack propagation exhibited by the miniaturized CT specimens was either due to the "…work hardening prevailing over loss of constraint in the un-cracked ligament in a side-grooved specimen, or to the inadequacy of J-integral to represent ductile crack extension in very small specimens." It was speculated that in a smaller specimen, the work hardening ahead of the crack tip is more extensive and leads to a reduction in tearing resistance. Alternatively, it was suggested that crack-tip opening displacement (CTOD) or crack-tip opening angle (CTOA) be used in lieu of the J-integral for small specimens. It was also proposed that a scaling approach, largely based on the theory of Turner [14] could allow the resistance curves obtained from the miniaturized specimens to be scaled-up. Some of the scaled-up curves were in reasonable agreement with the resistance curves obtained from the large specimens.

It bears emphasis that the Lucon et al. [13] study replicates the experience of Davies et al. [7] and Davies & Shewfelt [15] with testing of Zr-2.5Nb CANDU pressure tube material. In general, smaller samples yield lower resistance curves and consequently lower fracture toughness.

2.2.4 Comparison of the Specimen Geometries

Davies et al. [7] compared the resistance curves obtained using large and small CCTS with those obtained by testing centre-cracked panels and burst testing. The results are shown in Figure 6. In this figure, a crack extension of 6 mm corresponds to the onset of instability at maximum pressure in the burst test. The following observations deserve highlighting:

- up to a crack extension of 2 mm, resistance estimated from the W17 and W34-SPS CCTS agree reasonably well with the resistance from the burst test, although the former curves are slightly higher,
- from 2 mm to 6 mm crack extension, the W34-SPS CCTS toughness is approximately 10% higher than the resistance from the burst test,
- above 2 mm crack extension, the resistance curves obtained using the W17 CCTS deviate from the burst test data and become invalid at crack extensions greater than about 4 mm,

CanmetMATERIALS

- the resistance curve obtained using the centre-cracked specimen is significantly higher for any crack extension.
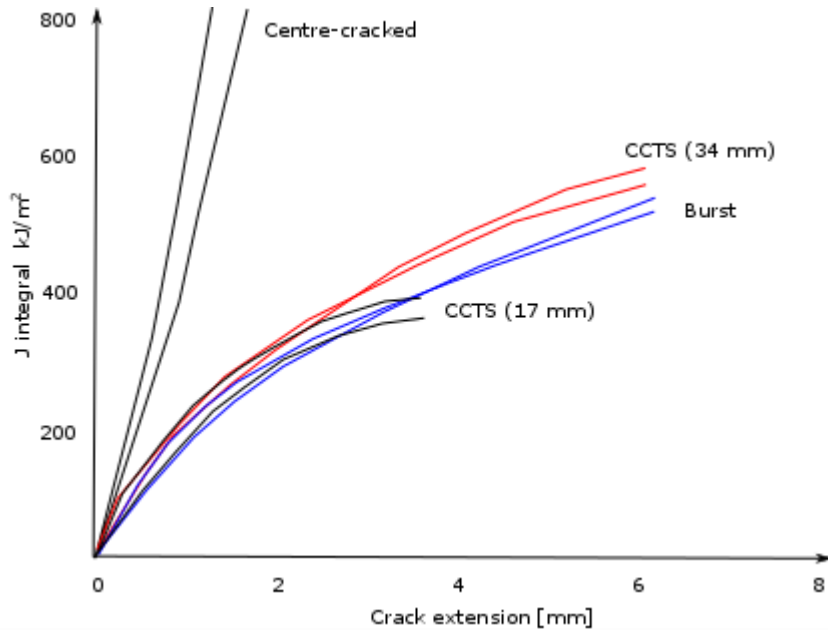

Figure 6: Comparison of J-resistance curves obtained using centre-cracked, W17 CCTS, W34-SPS CCTS, and burst tests; schematic reproduced from Fig. 14 in the article by Davies et al. [7].

From the discussion in this section, W34-SPS CCTS is an attractive alternative. Therefore, the next section presents finite element analyses of this geometry with stationary and growing cracks.

3 J-INTEGRAL PREDICTION FROM FINITE ELEMENT SIMULATIONS

The applicability of the ASTM procedure for the curved specimen geometry is addressed through extensive finite element (FE) analyses. In order to validate the finite element models and post-processing procedures presented in this work, a validation specimen is chosen and pertinent results for the stationary crack case are detailed. Then results regarding stationary crack analysis of both flat and curved C(T) geometries are presented.

Irradiated CCTS undergo extensive crack tunnelling during testing and the amount of crack front curvature violates the allowed crack front curvature in the ASTM Standard. However, this violation has been ignored, as methods for dealing with the effect of crack tunnelling on the J-integral are not available in the literature. It should be noted that the crack straightness criteria in ASTM E1820 have been shown to be highly conservative. In the current work, a damage mechanics approach was used to grow a crack with tunnelling followed by subsequent calculation of the J-integral. The method is briefly described in this section and used to predict the J-integral for a growing crack with tunnelling. Details of the J-integral calculation are provided in Appendix A.

The W17 CCTS has been studied using three-dimensional finite element analysis by Leitch & St Lawrence [16],[17]. The stress state at the crack tip and the J-integral were compared to those of FE analyses of a pressurize tube (PT) with an axial through-wall crack. Typical elastic-plastic properties for Zr-2.5Nb corresponding to about 300 °C were used to model the material of the PT. Leitch [17] concluded that two-parameter fracture mechanics indices such as J-T and J-Q could not be used to transfer the fracture toughness values between W17 CCTS and PT geometries. Examination of other indices such as plastic volume extent at the crack tip, and logarithm of the width of the plastic zone, did not permit transferability of fracture toughness either. The current work did not consider modelling PT geometry and focused on differences between the W17, W34-SPS, and W34-LPS CCTS geometries. The J-integral was the main parameter of interest and other fracture parameters such J-T and J-Q were not considered. It is suggested that modelling the constraint behaviour between PT and W34 CCTS geometries be considered in future work.

3.1 Validation of J-Integral Calculations from FE

To validate the J-integral prediction from finite element simulations, the Brooks & Scheider [18] C(T) geometry shown in Figure 7a, which conforms to ASTM E1820 recommendations, was first modelled. The implicit solver in the finite element package Abaqus [19] was used for the present study. The Finite Element (FE) computations carried out by Brocks & Scheider [18] also used Abaqus. An elastic-plastic material model with hardening properties of a 22NiMoCr37 steel were used in the model, as shown in Figure 7b.

Figure 8 shows the mesh of the validation specimen. Eight-node continuum elements with reduced integration (C3D8R) were used to mesh the domain. A fatigue precrack of 5 mm length (similar to that of Brocks & Scheider [18]) was modelled using the crack seam approach available in Abaqus. Displacement-controlled loading was applied to the top pin. Pins were modeled as 90-degree sectors. Rotation around the z-direction (parallel to the crack front) was permitted for both of the pins. The line of nodes in the center of the two pins was coupled to

CanmetMATERIALS ——————————————————————————————

reference points and the respective boundary and displacement conditions were applied to these reference points. Additionally, the vertical displacement and load in the reference point at the top was used for the J-integral analysis. Twenty-eight (28) elements through the thickness were used for the validation specimen model. 2D simulations were also carried out with a finer mesh, particularly at the crack tip, and it was found that the 3D mesh produced J-integral predictions slightly higher than the 2D case. For brevity, the 2D results are not presented.
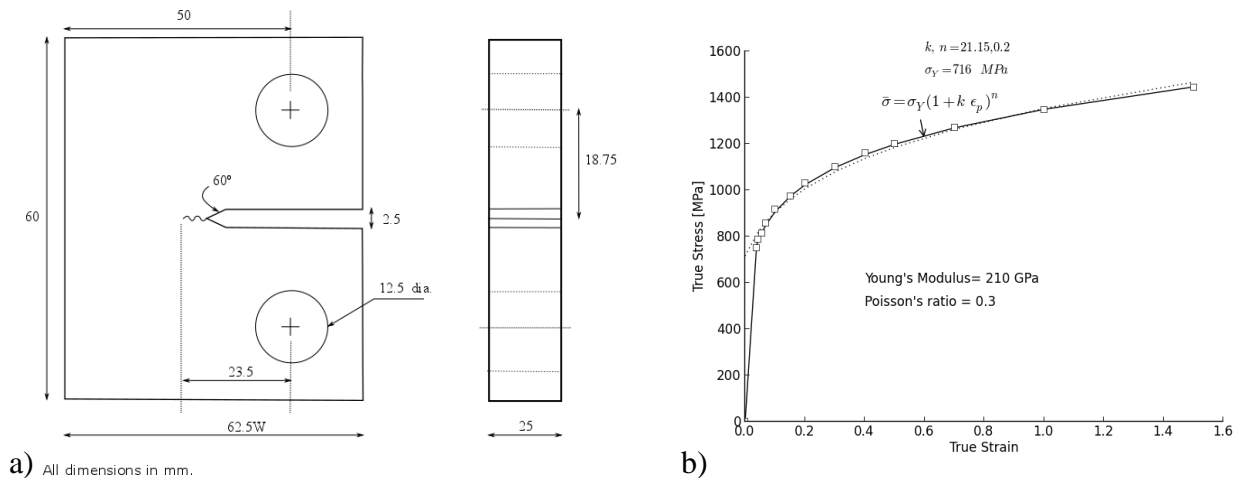
Figure 7: a) Compact tension specimen dimensions used for validation of J-integral calculations and b) stress-strain response used for FE model [18]
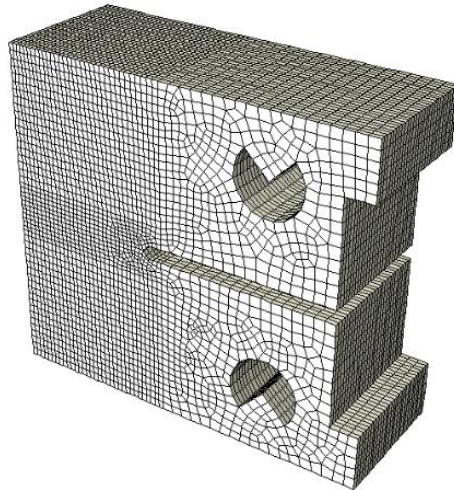

Figure 8: Finite element mesh of validation specimen

The J-integrals were obtained over several contours at each thickness interval around the crack tip using the built-in procedures in Abaqus that are computed using the domain integral method developed by Shih et al. [20] and Moran & Shih [21]. The results of the stationary crack front simulations are shown in Figure 9. There are four sub-plots given in the figure. Figure 9a shows the J-integral from simulation (solid lines) versus the (load-line) displacement of the specimen at 16 locations through the thickness of the sample, from the outer surface to the middle of the specimen.
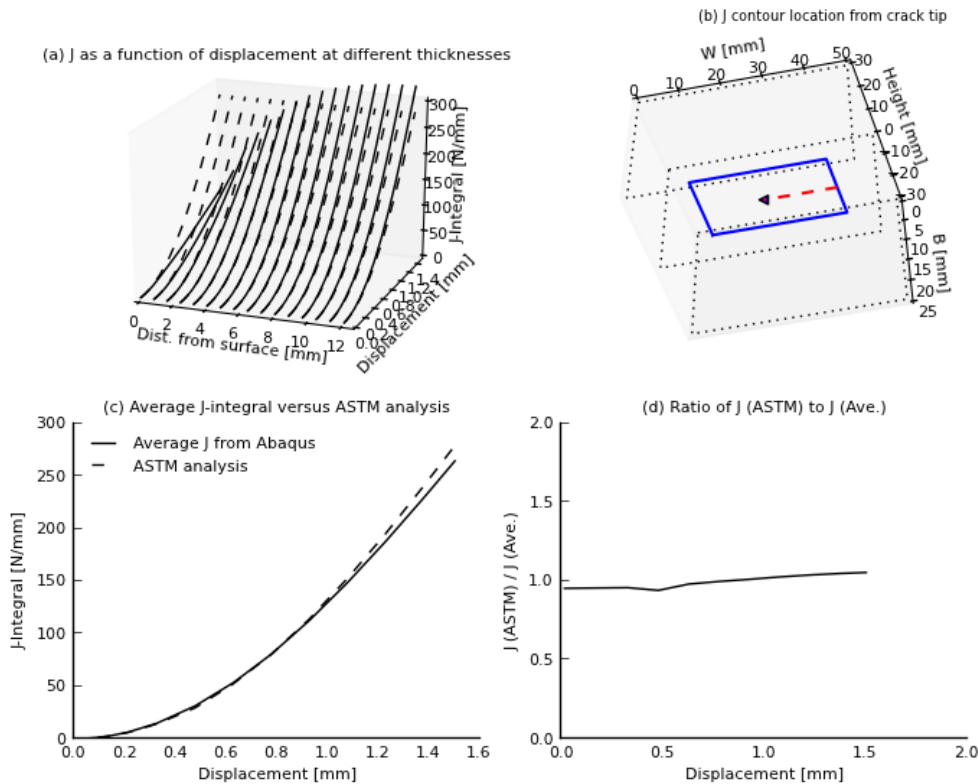
Figure 9: Results of FE computations for validation sample; dashed lines are from ASTM analysis; solid lines are from simulation.

Also shown in the figure are the corresponding J-integral values (dashed lines) calculated from ASTM E1820 equations using the force and displacement from simulation. The J-integral values from the ASTM equations are the same at each of the through-thickness locations, as it is a 2D solution. Figure 9a shows that at the outer surface the J-integral from simulations was much smaller than the J-integral from the ASTM equations, which was expected as plane stress conditions exist at the surface. Further towards the centre of the specimen the state approaches plane strain and the curves from the ASTM analysis agree reasonably well with the present curves obtained using domain integral analysis.

J-integrals were evaluated for contours approximately 10 mm from the crack tip, as depicted in Figure 9b. The J-curve obtained from the ASTM procedure is a global curve representing the entire structure, where as the J-curves computed by Abaqus are for each thickness interval. At a fixed distance from the crack tip all of the J-curves through the specimen thickness were averaged. As seen in Figure 9c, there was good agreement between the J-curve obtained using the ASTM analysis (dashed) and the J-curve obtained from the averaged domain integrals (solid). Figure 9d indicates that the ratio of the J-value calculated from ASTM and the J-value from simulation remains near unity with increasing displacement. The maximum difference at a displacement up to 1.6 mm was 5%. The curves agree with the values published in the report by Brocks & Scheider [18].

CanmetMATERIALS _____

3.2 Pressure Tube C(T) Specimens – Stationary Crack Analysis

The preceding models and post-processing indicated that for a flat C(T) specimen conforming to the geometry requirements outlined in ASTM E1820, the J-integral predicted from simulation corresponds well to the J-integral calculated from the ASTM analysis. In these next sections, the analysis will focus on the W17, W34-SPS, and W34-LPS CCTS geometries, both flat and curved, where the specimen dimensions deviate from those detailed in ASTM E1820, as detailed above. The Zr-2.5Nb pressure tube material was modeled as an elastic-perfectly plastic material with a yield strength of 600 MPa, a Young's Modulus of 100 GPa, and a Poisson's ratio of 0.4. The meshes for the W17 and W34-SPS CCTS are shown in Figure 10. The axial direction of the pressure tube is aligned with the 1- (or X-) direction and the transverse direction is aligned with the 2- (or Y-) direction. The current work assumed isotropic plastic deformation to describe the pressure tube material in the models. It is suggested that future work study the influence of anisotropic plastic deformation to assess any affect on the J-integral predictions.

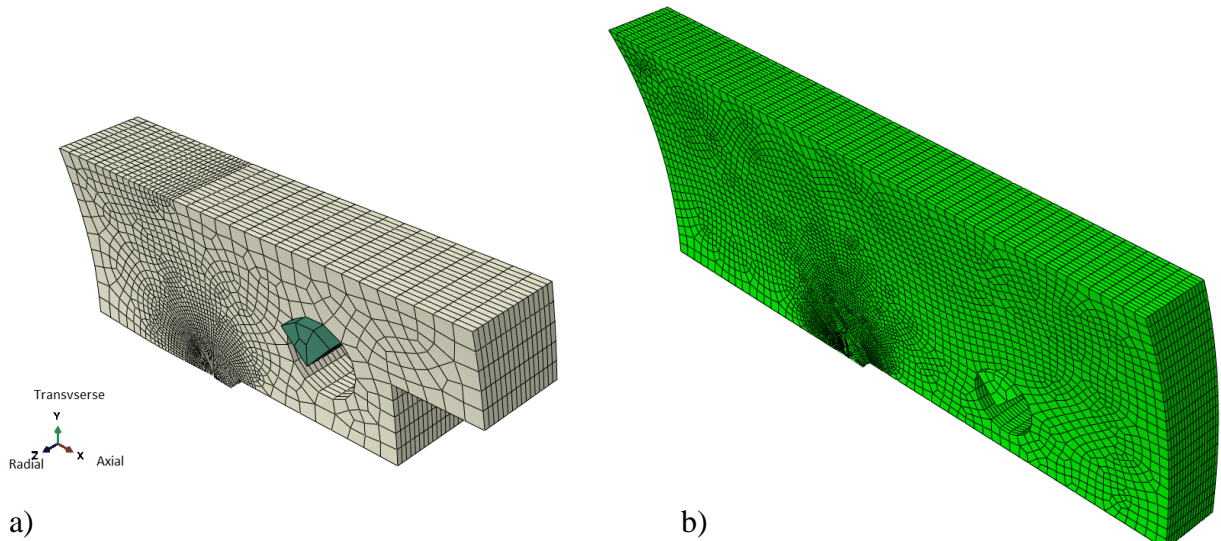a)   b)

Figure 10: Mesh details for a) W17 CCTS and b) W34-SPS CCTS

Figure 11 and Figure 12 show similar predictions between the flat and curved W17mm C(T) specimens, respectively. The J-integrals are given at various through-thickness locations where the outer surface is at a distance of zero and the inner surface is at a distance of 4.2 mm. For the flat geometry, the ASTM procedure overestimates the J-curve calculated by the domain integral analysis by approximately 8% at a displacement of 1.0 mm. For the curved geometries, the force and displacement predicted from simulation were also used to calculate the J-integral using the ASTM analysis. If the specimen curvature is incorporated in the model the ASTM analysis overestimates the J-integral by approximately 9% at a displacement of 1.0 mm. Results presented in Figure 13 further emphasize that specimen curvature has little effect on the J-integrals. Changes in J-values on account of curvature are predicted to be less than 1% relative to the flat specimen for both the ASTM procedure and the domain integrals predicted from simulation.
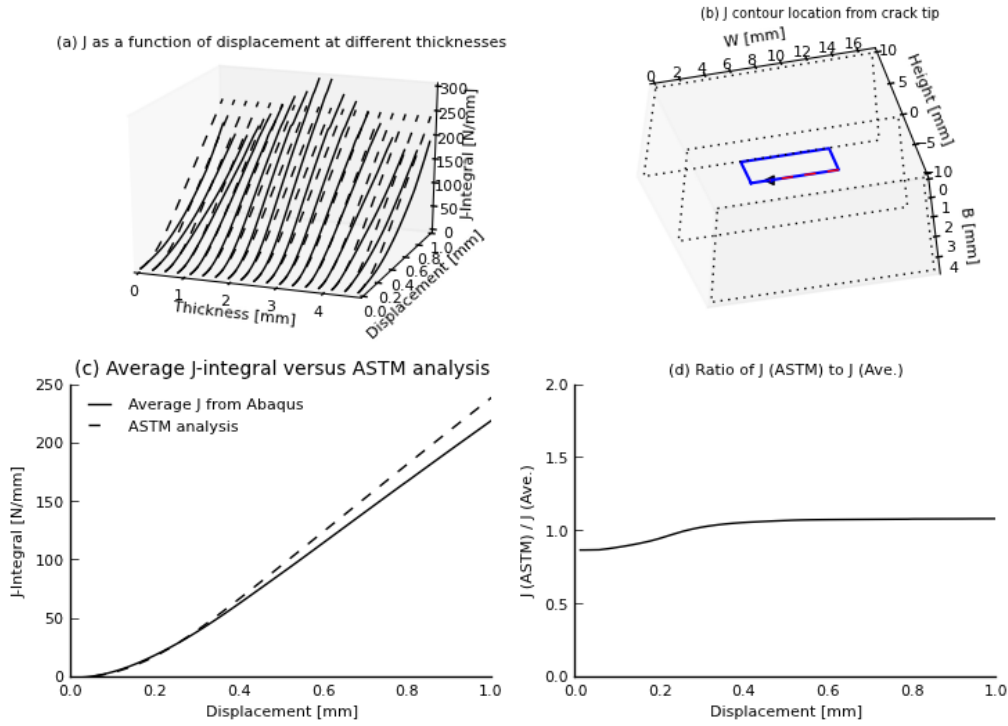
_____
CanmetMATERIALS

Figure 11: Results of FE computations for W17 flat C(T) with stationary crack; dashed lines are from ASTM analysis; solid lines are from simulation.
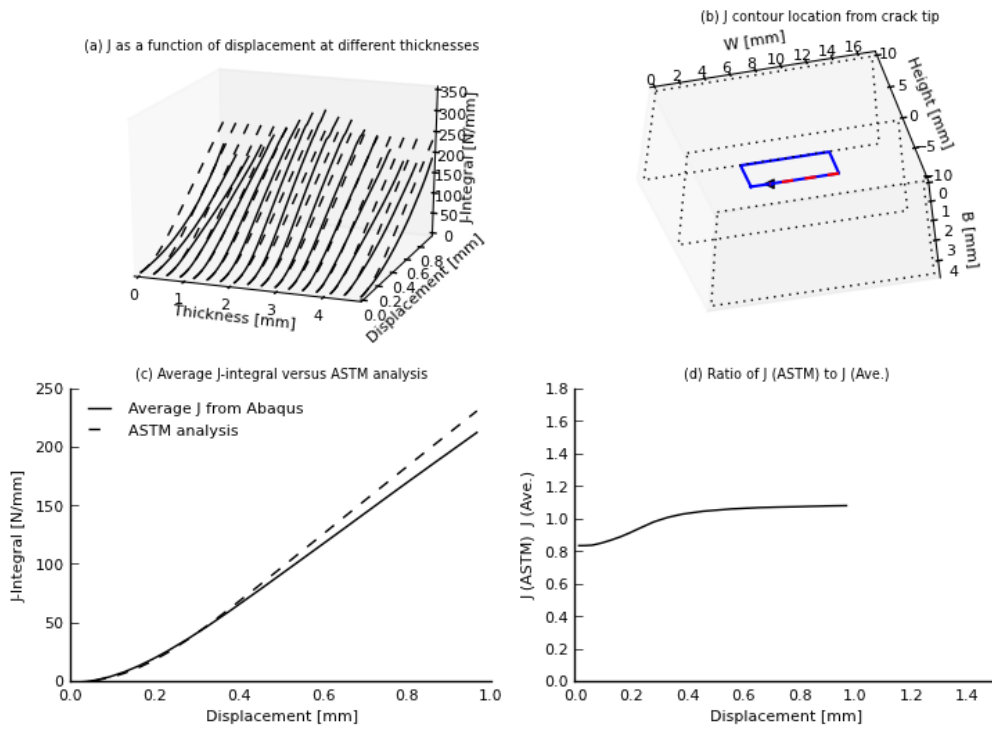

Figure 12: Results of FE computations for W17 CCTS with stationary crack; dashed lines are from ASTM analysis; solid lines are from simulation.
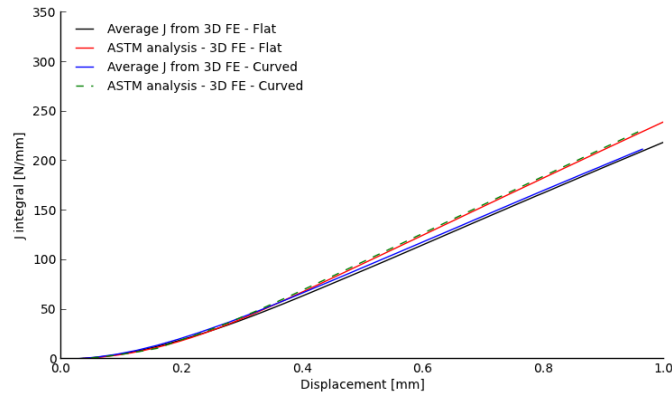
Figure 13: Comparison of J-curves from flat- and curved- specimen models; curves obtained using ASTM procedure are compared with the average J-curves.

Fracture results are shown in Figure 14 for the W34-SPS CCTS geometry with a stationary crack. The ASTM procedure initially under-predicts the J-values but then over predicts the J-values by about 8% at a displacement of 1.0 mm. Stationary crack simulations were also performed for the W34-LPS CCTS geometry. Figure 15 shows the ratio of the J-integral values computed using the ASTM E1820 procedure to the average J-integral calculated from the domain integrals. As with the W34-SPS prediction, the J-integral is initially under-estimated by amounts of about 20 % but with increasing displacement the trend transitions to an over-estimation by amounts ranging up to about 20% at 1.0 mm of displacement. This suggests that it is beneficial to use smaller pin spacing to reduce the influence of curvature.
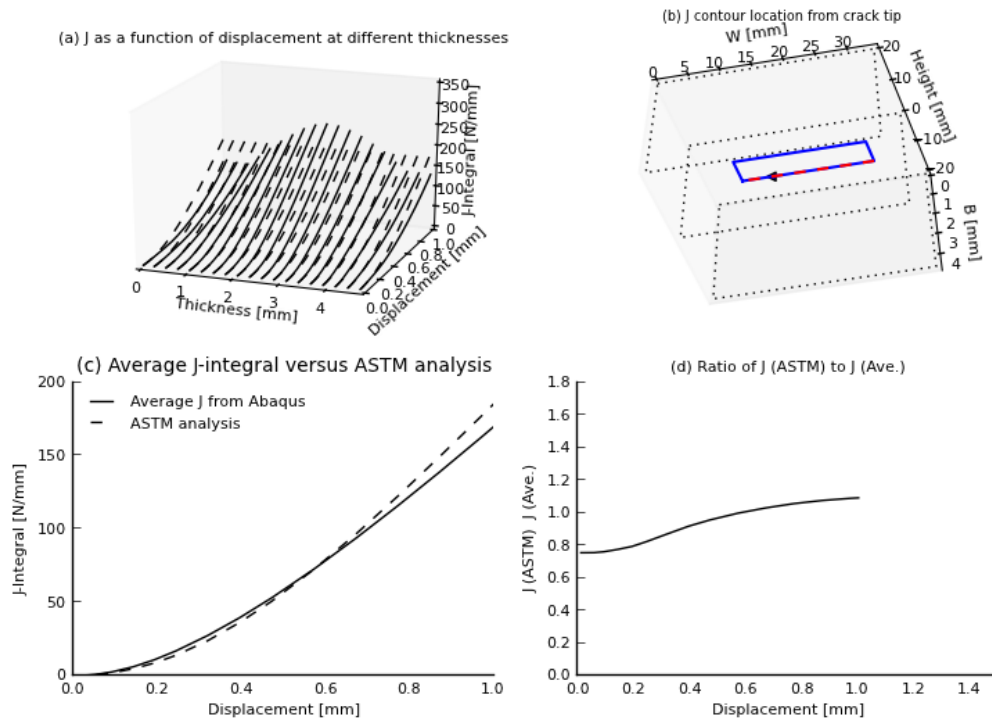

Figure 14: Results of FE computations for W34-SPS CCTS with stationary crack; dashed lines are from ASTM analysis; solid lines are from simulation.
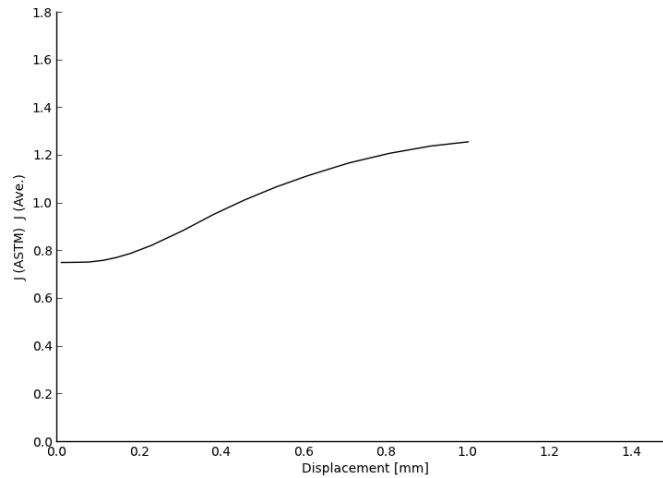
_____ **CanmetMATERIALS**

Figure 15: Ratio of J-integrals obtained using the ASTM procedure and the domain integral method for W34-LPS CCTS

Stress triaxiality (mean stress / effective stress) and effective plastic strain versus specimen thickness from the W17 and W34-SPS CCTS simulations are compared in Figure 16. At a distance of $2J/\sigma_y$ from the crack tip (also used by Leitch & St Lawrence [16]) there is no appreciable difference in triaxiality through the specimen thickness for the large and small size. At J = 180 N/mm, the plastic strain in the plastic zone is somewhat greater at the mid-thickness of the smaller specimen.
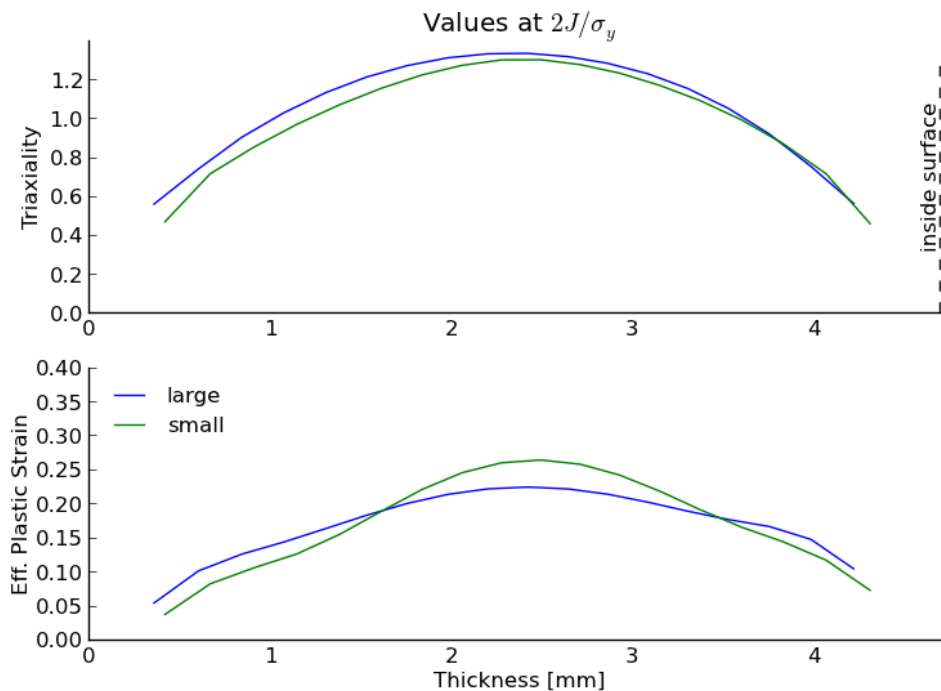

Figure 16: Top: Comparison of triaxiality in W17 and W34-SPSl CCTS for a similar value of $2J/\sigma_y$. Bottom: comparison of plastic strain through the specimen thickness for J=180 N/mm.

CanmetMATERIALS

3.3 Growing Crack Analysis Procedure

It is well known that crack-front curvature affects the evaluation of the J-integral, as detailed in [22]. Both irradiated and un-irradiated curved C(T) specimens demonstrate significant crack front tunnelling (in violation of the validity requirements in ASTM standard E1820). For example, see Chow & Simpson [3] for fractographs of curved cracks. Consequently, it was of importance to compare the J-integral predicted from a growing, tunnelling crack with the corresponding J-integral from the ASTM Standard. To study a growing crack with tunnelling a damage mechanics approach was used, which was based on the method described by Oh et al. [23] and enhancements reported by Kim el al. [24]. In the model, damage initiation was assumed to depend on stress triaxiality and damage evolution increased with further strain resulting from material displacement. The failure strain, ε_f, at initiation was given by,

$$\varepsilon_f = A + B exp(-1.5T) \tag{1}$$

where A and B are constants and T is the stress triaxiality given by the mean stress divided by the effective stress. The triaxiality factor of 1.5 is from the model due to Rice & Tracey [25]. In the current work, A=0.1 and B=3.29, which were selected to provide realistic crack propagation in the simulations. The initiation strain versus triaxiality response is depicted in Figure 17a.
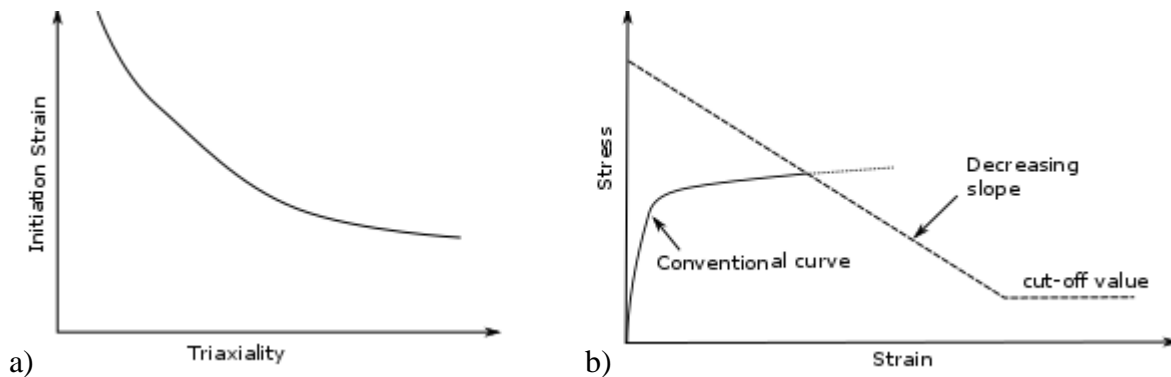

Figure 17: a) Schematic of failure strain as function of triaxiality and b) Schematic illustrating the stress relaxation scheme used to model degradation of material strength.

Damage evolved as $dD = d\varepsilon_p/\varepsilon_f$ where ε_p is the effective plastic strain. When the damage was equal to a critical value, $D = D_c$, the strength in an element was reduced to a low, near zero stress value. To prevent computational instabilities, the strength reduction was carried out using a relaxation procedure that had a decreasing slope. Figure 17b presents a schematic of the relaxation procedure. Oh et al. [23] recommend a cut-off stress value of 5 MPa for the strength and Kim et al. [24] suggest setting the elastic modulus to 100 MPa. In the current work, D_c was equal to 0.76, which was determined by trial-and-error so as to balance speed of computation with extent of crack growth. The procedure was implemented in the Abaqus using a combination of UHARD and USDFLD subroutines.

3.4 Pressure Tube C(T) Specimens - Growing Crack Analysis

Finite element models of W17 and W34-SPS CCTS for the growing crack analysis were similar to the models for the stationary crack simulations. A yield strength of 600 MPa was again used, but slight hardening response was specified to prevent computational instability during crack growth. The model comprised 18 elements through the thickness with the element size being about 0.25 mm for elements on the crack plane for the W34-SPS geometry. Figure 18 shows the predicted amount of crack tunnelling in the W17 and W34-SPS growing crack simulations. The area in grey represents elements that have exceeded the critical damage level specified in the model. As can be seen in the figure, a significant amount of crack tunnelling was captured in the models demonstrating that the effect of crack tunnelling on the predicted J-integral can be adequately assessed. One difference with the growing crack analysis compared to the stationary crack analysis in the calculation of the J-integral from ASTM was the addition of the crack-growth correction factor.

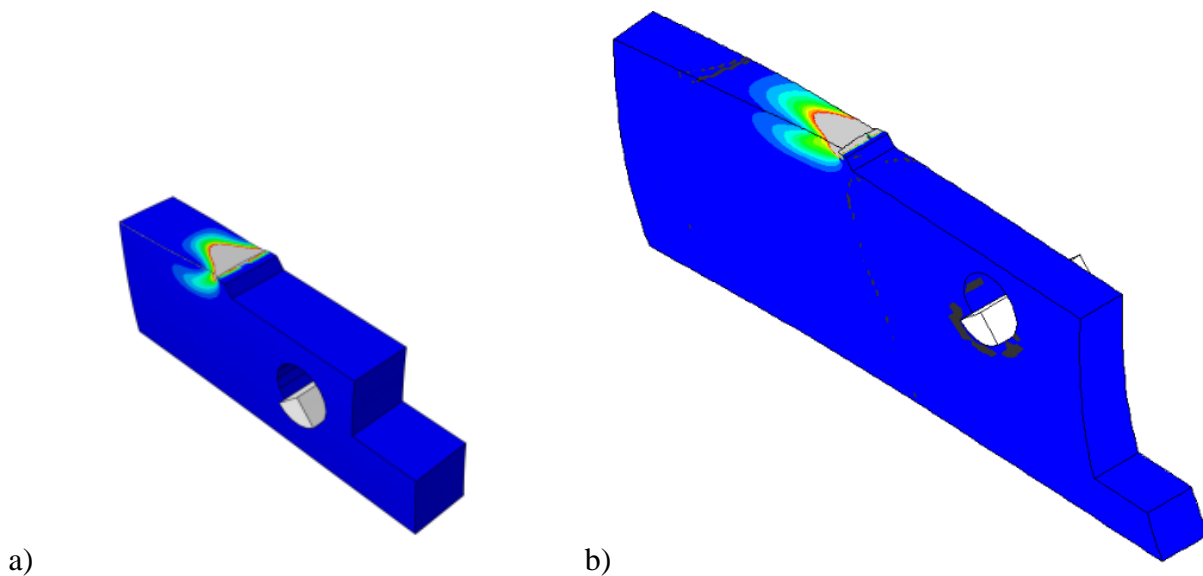a)   b)

Figure 18: Predicted tunnelling along crack plane from crack growth simulation of a) W17 CCTS and b) W34-SPS CCTS

The fracture results of the growing crack analysis are shown in Figure 19 and Figure 20 for the W17 and W34-SPS CCTS, respectively. The load-line displacement on the horizontal axes (as in previous figures) has been replaced with crack extension. The contour selected for evaluation of J (shown in panel (b) of the figure) is chosen so as to well envelop the plastic zone at the crack tip. For the W17 CCTS, the ASTM procedure over predicts the J-integral from simulations by approximately 12% at a crack extension of 1.8 mm. This is compared to an over prediction of about 9% for the stationary W17 analysis at a crack extension of 4.0 mm. For the W34-SPS case, the ASTM analysis yields a resistance curve that is in excellent agreement with the average domain integral with on over prediction of about 5% at a crack extension of 4.0 mm.
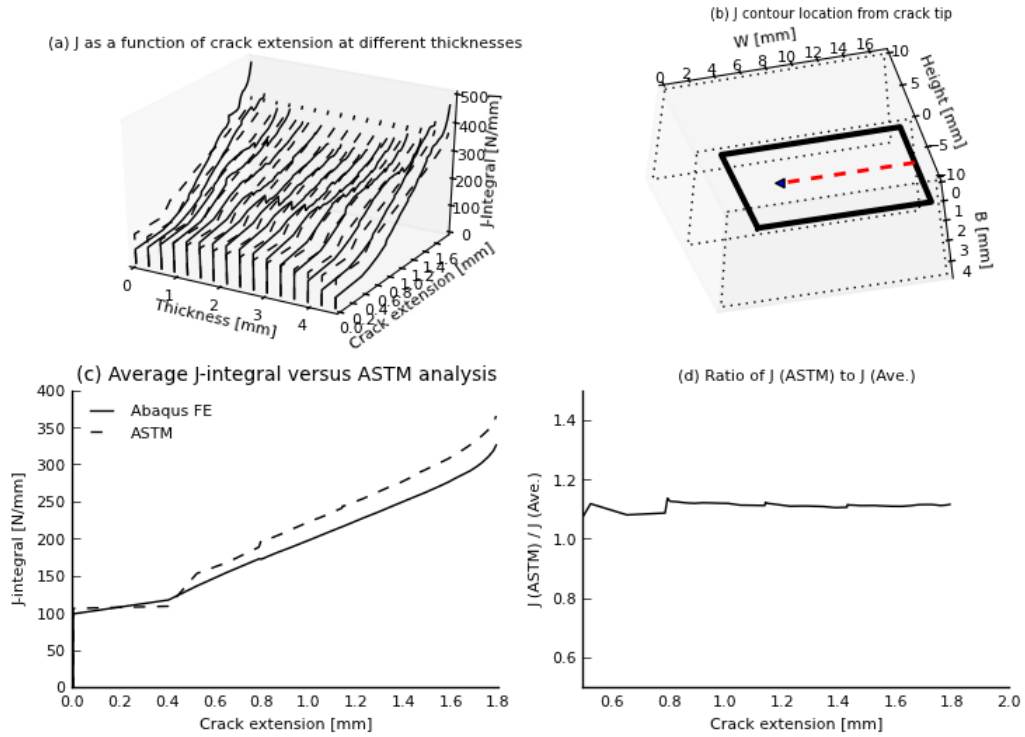
CanmetMATERIALS _____

Figure 19: Results of FE computations for W17 CCTS with growing crack; dashed lines are from ASTM analysis; solid lines are from simulation.
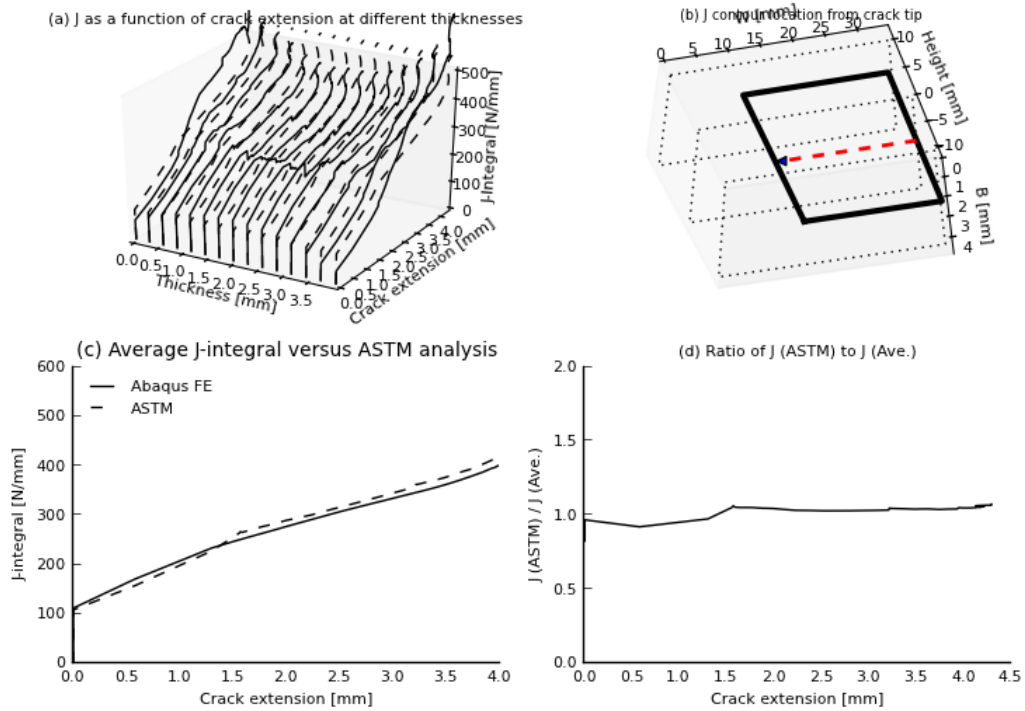

Figure 20: Results of FE computations for W34-SPS CCTS with growing crack; dashed lines are from ASTM analysis; solid lines are from simulation.

3.5 Summary of FE Simulations

A summary of the difference between the J-integral calculated from the ASTM analysis relative to the J-values calculated from simulation using the domain integral procedure of Abaqus is presented in Table 1. The initial *a/W* ratio of the simulations is also given in the table. The J-Simulation value was based on an average of the J-integral value calculated for each thickness contour corresponding to the maximum crack-tip position. The crack extension at a given thickness may have been slightly less than the maximum value due to crack-tip tunnelling. The J-ASTM value was calculated using the maximum crack-tip position corresponding to the average value used to calculate J-Simulation. A 5% over prediction was calculated for the benchmark specimen which conformed to all geometry requirements in ASTM E1820. An 8% difference was calculated for the W17 flat geometry, indicating that slight violations of the geometry recommendation in ASTM E1820 have only a small influence on the J-integral. When comparing the W17 C(T) flat and curved geometry simulations with a stationary crack it is seen that a 1% difference resulted. This indicates that specimen curvature has little influence on the J-integral for the W17 geometry. W17 CCTS simulations of a stationary versus a growing crack indicated a 3% difference showing that crack tunnelling did not significantly influence the J-integral. Simulations of the W34-SPS and W34-LPS CCTS geometry with a stationary crack indicated an 8% and 20% over prediction, respectively. For W34-LPS CCTS, the 20% over prediction was at the end of the simulation with larger applied displacements. For the W34-SPS growing crack simulation, the ASTM analysis yielded a resistance curve that was in excellent agreement with the average domain integral values. This suggests that it is beneficial to use the smaller pin spacing in the W34-SPS CCTS relative to the W34-LPS CCTS.

Table 1: Per cent difference of the J-integral between ASTM analysis and simulation domains

Compact Tension Specimen	Geometry	Crack Front	a_0	W	a_0/W	J-ASTM relative to J-Simulation[*]
benchmark	flat	stationary	23.5	50	0.47	5%
W17	flat	stationary	8.25	17	0.49	8%
W17	curved	stationary	8.25	17	0.49	9%
W34-SPS	curved	stationary	15	34	0.44	8%
W34-LPS	curved	stationary	15	34	0.44	20%
W17	curved	growing	7.75	17	0.46	12%
W34-SPS	curved	growing	14.6	34	0.43	5%

* - at end of simulation

CanmetMATERIALS

4 FRACTURE TOUGHNESS TESTING OF CCTS

4.1 Material

A Zr-2.5Nb pressure tube with a length of 6.44 metres was procured from Nu-Tech Precision Metals. This non-reactor grade pressure tube met all of the specifications of a reactor-grade pressure tube [26]. The pressure tube material was subjected to a quad-melt process such that it would be expected to have a low concentration of chlorine and a high fracture toughness prior to irradiation [27]. One difference with this pressure tube was that the thickness was 4.4 mm compared to the 4.2 mm thickness of pressure tubes used in CANDU reactors. Several CCTS were machined from a section taken from one end of the pressure tube as depicted in Figure 21. Three W17, three W34-LSP, and two W34-SPS CCTS were tested from specimens machined from one end of the pressure tube. An additional four transverse tensile specimens were machined as detailed in the next section.
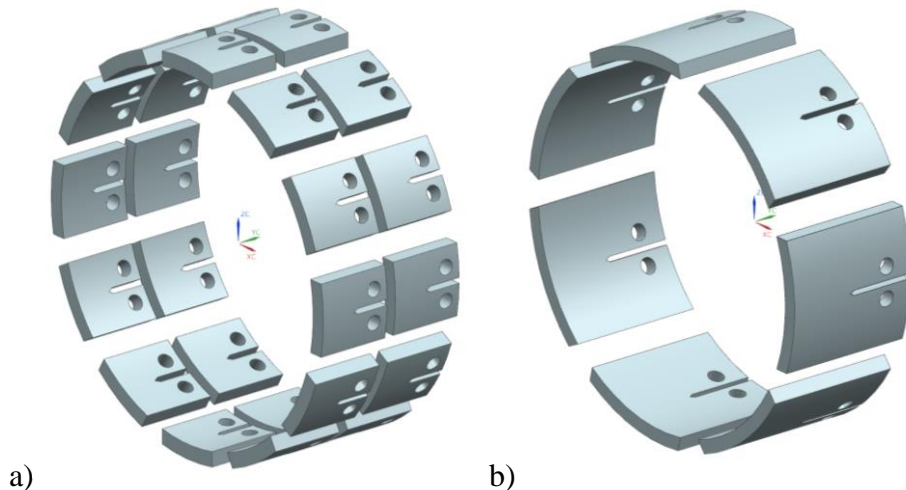

a)   b)
Figure 21: Depiction of orientation of CCTS machined from rings of the Zr-2.5Nb pressure tube a) W17 and b) W34-modified geometries

4.2 Tensile Stress vs. Strain Curves

For Zr-2.5Nb pressure tube material, it is typical to test specimens with the transverse direction of the tube corresponding to the major stress or strain axis of the sample [28]. To achieve a gauge length of 10 mm during testing, a unique Transverse Tensile (TT) geometry is machined from the pressure tube as shown in Figure 22. The thickness, width, and gauge length of the TT specimens were 2 mm, 4 mm, and 10 mm, respectively. The custom grips used to test TT specimen geometry in [28] were not available in the current work. Tensile specimens with a wide clamping region (refer to Figure 22b) were machined from the pressure tube. The gauge length (2 x 4 x 10 mm) was the same as the specimen used in [28]. The engineering stress versus strain response for three unirradiated Zr-2.5Nb transverse tensile specimens tested at a rate of 0.01 mm/s at room temperature are shown in Figure 23. Typical response for un-irradiated Zr-2.5Nb material at room temperature was measured, with the peak stress occurring at low strain followed by a gradual decrease of stress until failure. The ultimate tensile strength was measured to be 856 MPa and is required in the calculation of the fatigue precracking load limits as detailed in the next section.

_____ **CanmetMATERIALS**

a)   b)
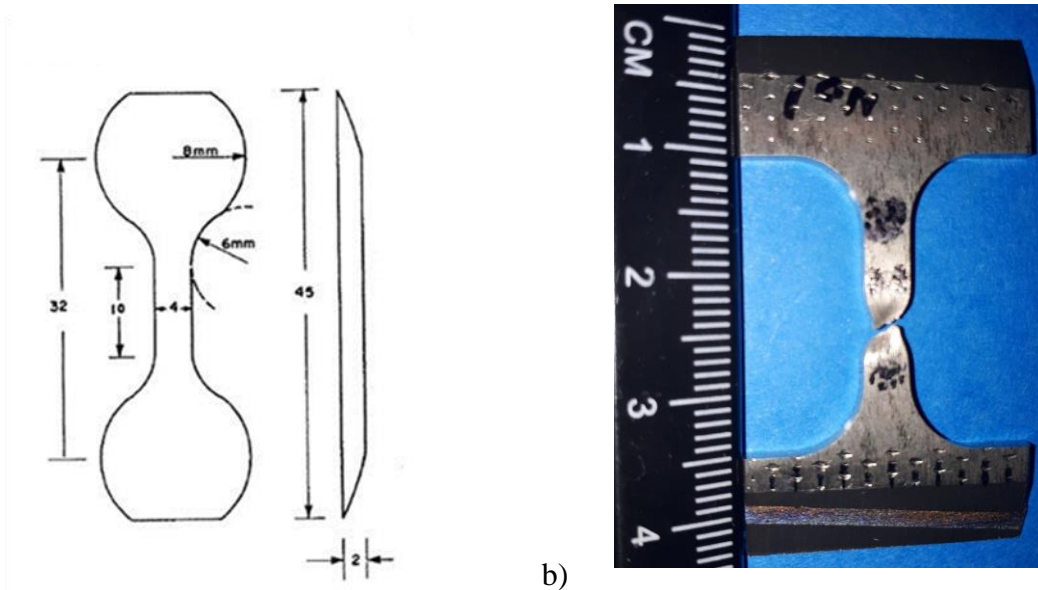
Figure 22: Transverse Tensile (TT) specimen used by Himbeault [28] and b) geometry used in current work
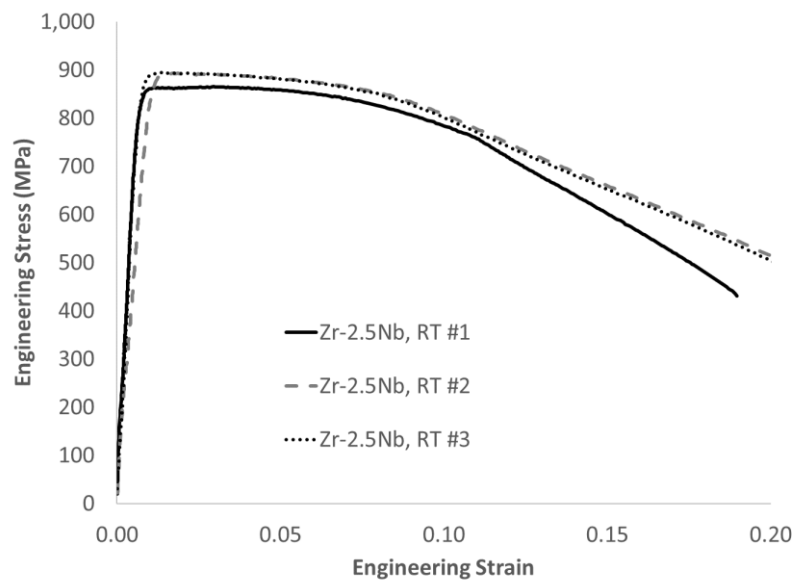

Figure 23: Room temperature stress vs. strain response for unirradiated Zr-2.5Nb

4.3 CCTS Test Procedure

There are three stages to performing the compact tension test. The first step is to fatigue the specimen to grow a sharp crack from the initial notch at $a/W = 0.4$ to $a/W \approx 0.5$. The second step is to perform the stable crack growth fracture test under displacement control. The third step is to heat tint the sample, to clearly distinguish the fatigue and ductile crack growth regimes, and then subject the sample to fatigue loading till the sample fails.

CanmetMATERIALS

4.3.1 Grip Design

A custom set of grips was machined for each of the three CCTS geometries. Grips with arms of different thickness were machined to ensure that the load line is centred when the curved fracture specimens are loaded in the grips. The offset can be seen in Figure 24a for the W34-modified case. A flat region was machined in the hole for the load pins, as seen in the side-view of Figure 24b, to provide rolling contact between the specimen and the pins. Details of the grips for the three geometries are given in Appendix C.
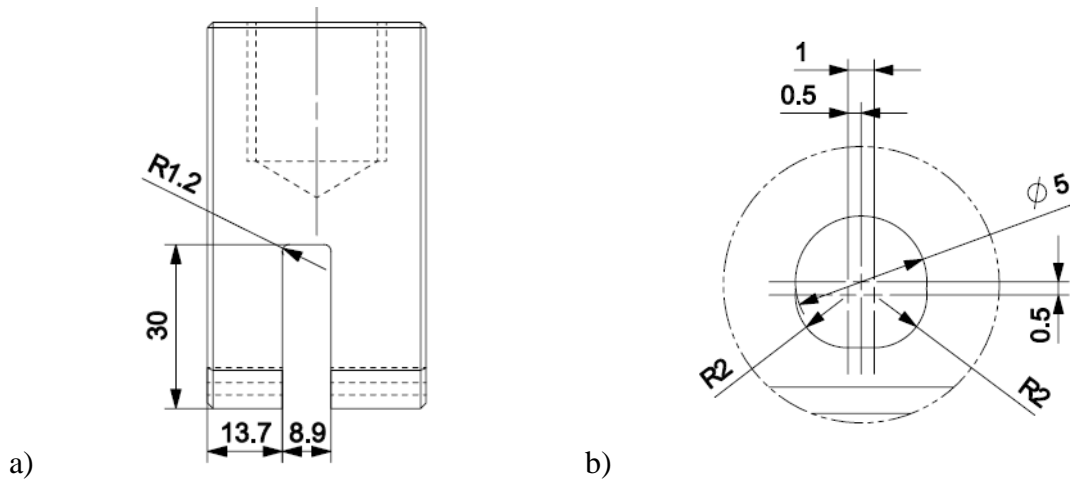

a)   b)

Figure 24: CCTS grips for W34-modified test geometry a) front-view of grip and b) side-view of pinholes; dimensions in mm.

4.3.2 Fatigue Precracking

To ensure a small plastic zone size at $a/W = 0.5$, the load during fatigue precracking was minimized. ASTM E1820 suggests using $0.7K_{max}$ where K_{max} is given by

$$K_{max} = \left(\frac{\sigma_{YS}^f}{\sigma_{YS}^T}\right)\left(0.063\sigma_{YS}^f\right) \text{ MPa}\sqrt{\text{m}} \tag{2}$$

with σ_{YS}^f in MPa for the first 50% of fatigue crack growth; Eq. (2) yields $0.7K_{max} = 37.7$ MPa√m with $\sigma_{YS}^f = \sigma_{YS}^T = 856$ MPa. ASTM E1820 recommends that this value be reduced by a factor of about 0.6 for the final half of the fatigue crack growth [4]. A Stress Intensity Factor (SIF) of 37.7 MPa√m is larger than the initial SIF value of 20 MPa√m for the fatigue precracking operation reported by Chow and Simpson [3]. In the current work, an initial SIF value of 20 MPa√m was used for precracking followed by a reduction to 16.3 MPa√m and a final reduction to 12.7 MPa√m, as shown in Figure 25. An R-ratio of 0.1 was used for all fatigue operations [4] at a frequency of about 10 Hz.
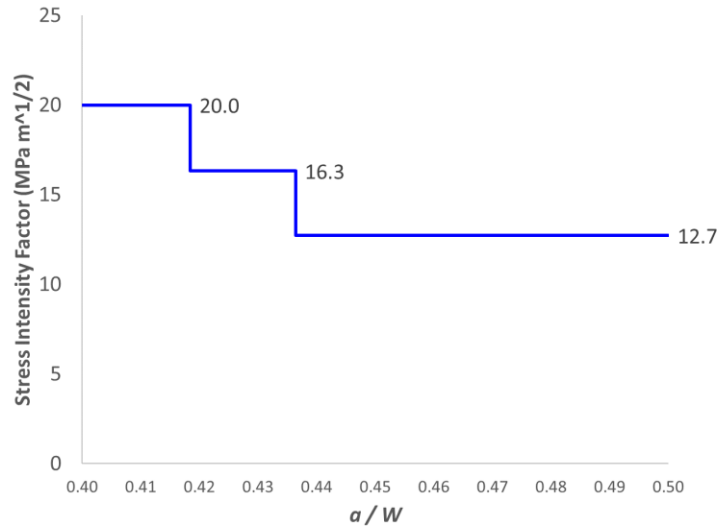
Figure 25: Stress intensity factor vs. crack length during fatigue precracking for the W17, W34-SPS, and W34-LPS CCTS

The Direct Current Potential Drop (DCPD) technique was used to measure the crack size from $a/W = 0.4$ to $a/W = 0.5$ from the voltage increase that was monitored during fatigue precrack growth. A normalized PD value was calculated based on crack voltage and reference voltage. The approximate locations of the voltage and current probes are shown in Figure 26. An equation to relate voltage increase to crack growth could not be found in the literature for Zr-2.5Nb. Consequently, the Johnson equation given in ASTM E647-05 [29] was initially used in the present work to relate voltage increase to crack extension. The minimum load level during precracking corresponded to a SIF value of 12.7 MPa√m for at least the final 50% of fatigue crack growth. The normalized PD value (voltage / initial voltage, V/V_0) at which the precracking was stopped was then adjusted in a trial and error manner for each CCTS test until an a/W ratio of about 0.5 was achieved..
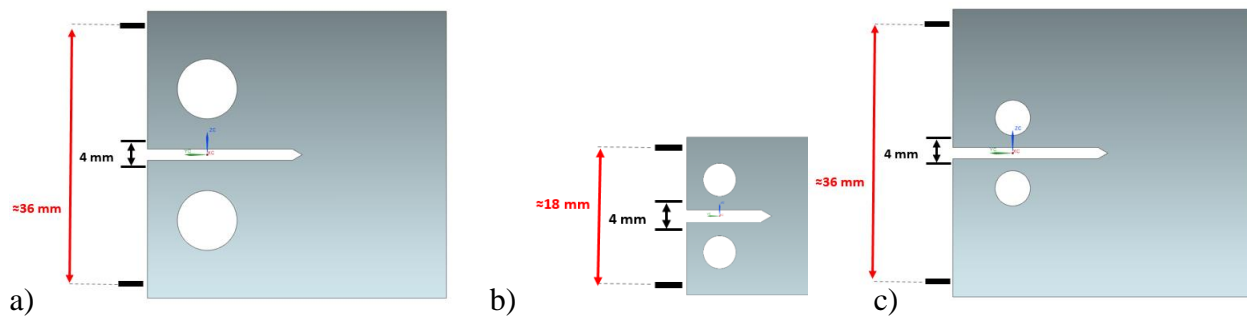
Figure 26: Probe locations for voltage (inner pairs of locations) and current (outer pairs of locations) for a) W34-LPS, b) W17 and c) W34-SPS CCTS geometries

Initially, precracking was conducted using straight pins but it was found that the fatigue crack front was significantly curved. Consequently, tapered pins with a 1° taper were considered for the precracking operation. The pins were wrapped in Teflon tape for electrical isolation. The same pins were used for both the precracking operation and the stable growth fracture test.

CanmetMATERIALS

4.3.3 Stable Growth Fracture Regime

After precracking, each specimen was tested under displacement control at a rate of 0.5 mm/min to obtain stable crack growth. This displacement rate corresponds to an initial rate of increase of SIF of about 1 MPa√m /s [30]. The fracture test was stopped when the peak load decreased by about 50% with a target crack extension of between 3 to 4 mm for the W17 geometry and between 6 to 8 mm for the W34-SPS and W34-LPS geometries. The force, actuator displacement, and voltage (from DCPD measurement) were recorded for each test. The voltage increase was related to crack extension during post-test analysis.

Owing to extraneous compliance, the actuator displacement does not exactly correspond to the Load Line Displacement (LLD) of the CCTS, which is required for the J-R curve. Compliance arises from mechanical stiffness in the test system and bending of the pins during loading. Clip gauges are often used in fracture toughness tests to obtain an accurate LLD measurement but were not used in the current work. Rather, a non-contact video extensometer was employed to measure deformation of the CCTS. The front view for a W17 CCTS test is shown in Figure 27 with the video extensometer gauge length being about 10 mm. The black speckles seen on the specimen centred between the grips were required for the video extensometer measurements.
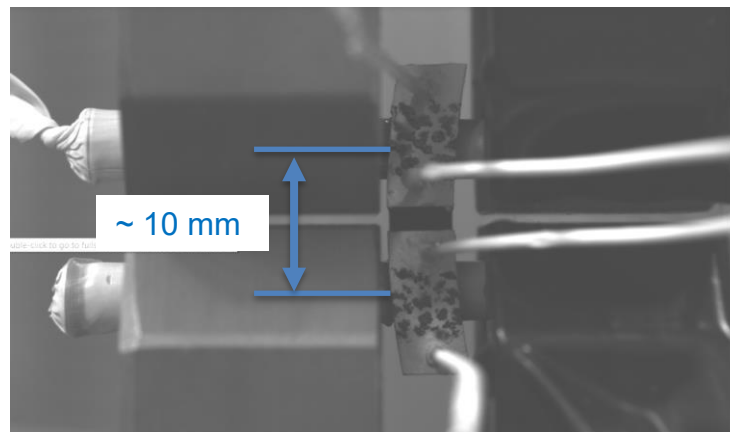
Figure 27: Location on the W17 geometry at which the displacement was measured using a video extensometer

The force versus displacement response measured from the Linear Variable Differential Transformer (LVDT) sensor on the load frame and the video extensometer are compared in Figure 28 for a W17 test geometry. It can be seen that there is a difference, particularly during initial loading, between the two displacement measurements. The data was corrected for compliance with good agreement up to maximum load between the video extensometer data and the LVDT data corrected for compliance. After maximum load, the data that was corrected for compliance did not capture the video extensometer data exactly. This could result in some fluctuation, after maximum load, in the calculation of the J-R curves.

_____ **CanmetMATERIALS**

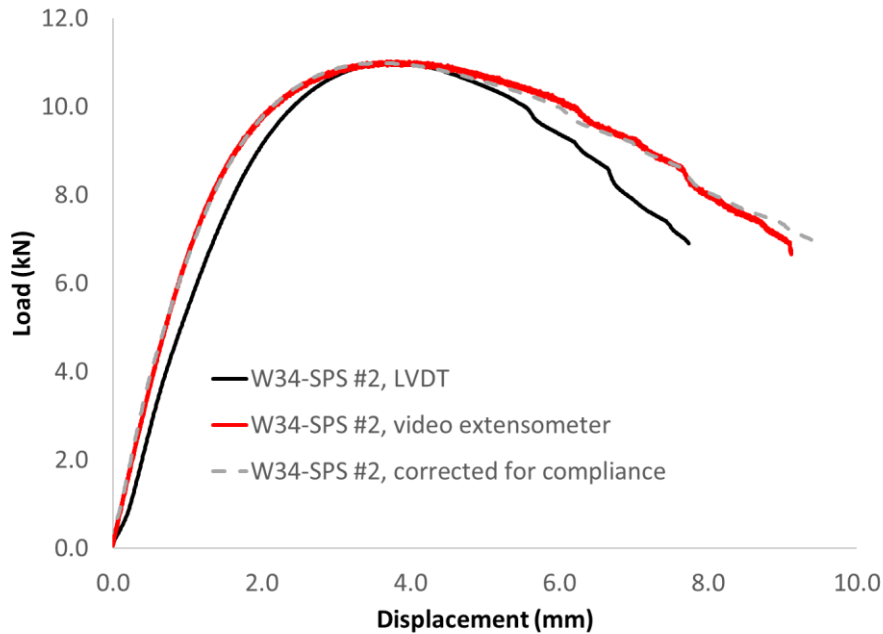Figure 28: Force vs. displacement response based on displacement measurement from load frame and video extensometer

4.3.4 Failure of the Remaining Ligament

After the stable crack growth regime, the specimens were heat tinted at 300 °C for about 0.5 hours to clearly distinguish the precrack and fracture surfaces. After heat tinting, the specimens were further fatigued at an R-ratio of 0.7 to complete failure at about 50% of the load at the end of the stable growth test.

4.4 Post-Test Analysis

After the test was completed an image was taken of the crack plane. This was used to determine the crack extension using the nine-point procedure outlined in ASTM E1820 [4]. In this procedure, an average of the inner and outer crack extensions (taken at through-thickness location of $0.005W$ from the side of the specimen) was averaged with crack extension measurements from an additional seven locations centred about the specimen mid-plane. The nine crack length measurements are shown for a typical W17 Zr-2.5Nb specimen in Figure 28 where an average crack extension of 2.94 mm was calculated.

Point	W17, Zr-2.5Nb #4	
near-surface length 1	2.44	mm
near-surface length 2	2.47	mm
near-surface average	2.46	mm
pt1	2.61	mm
pt2	2.92	mm
pt3	3.16	mm
pt4	3.44	mm
pt5	3.3	mm
pt6	2.89	mm
pt7	2.72	mm
average	2.94	mm

a)   b)
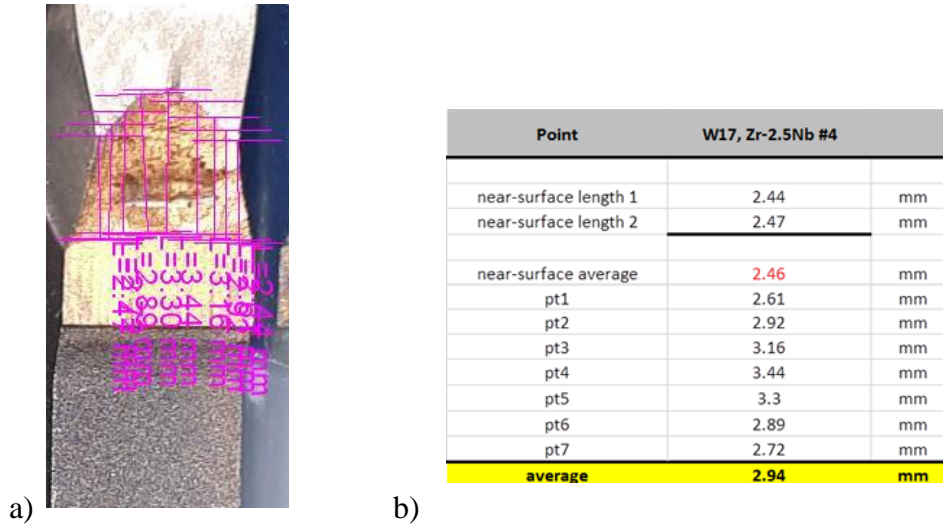
Figure 29: a) Crack plane image used to determine crack extension from nine measurements and b) corresponding average crack extension of 2.94 mm

A linear relationship was used to relate the normalized PD measurement to the average crack extension according to,

$$\alpha = \frac{\Delta a_f / W}{\left(\frac{V_f - V_0}{V_0}\right)} \tag{3}$$

where Δa_f is the average crack extension measured from the crack plane images, and V_0 and V_f are the normalized initial and final voltage values measured during the fracture test. The assumption of linearity was not addressed in the current work.

5   CCTS RESULTS – ZR-2.5NB

5.1 Test Matrix

The results from eight CCTS tests will be detailed in this section, as shown in Table 2. There were no major issues encountered during testing, but there were a couple of items of note. For the three W17 CCTS, the voltage probes for the potential drop measurement fractured just prior to the end of the stable crack extension. Consequently, some minor extrapolation was required to determine the final voltage value that corresponded to the final measured crack extension. As discussed in Appendix C, there was some pin bending observed for the W34-SPS CCTS but this was not expected to have a significant influence on the fracture response.

Table 2: W17, W34-SPS, and W34-LSP Test Matrix

Sample ID	Initial *a/W*
W17 #1	0.53
W17 #2	0.52
W17 #3	0.53
W34-SPS #1	0.50
W34-SPS #2	0.51
W34-SPS #3	0.51
W34-LPS #1	0.51
W34-LPS #2	0.52

5.2 Force, Displacement, and Crack Extension

The force versus displacement (corrected for compliance) responses for three W17 CCTS, three W34-SPS, and two W34-LPS CCTS are shown in Figure 30. The force versus crack extension response is shown in Figure 31. Overall, the results indicate good repeatability between tests for the same configuration. The results for the W34-SPS and W34-LPS are very similar with Figure 30 indicating a slight discrepancy upon initial loading which was attributed to the difference in pin spacing (10 mm for SPS and 18.7 mm for LPS). After the load attained peak value, there was some difference in the displacement response between W34-SPS and W34-LPS CCTS. Oh et al. reported on the force versus displacement response measured from a 17 mm CCTS for unirradiated Zr-2.5Nb pressure tube material at room temperature with *a/W* = 0.47 [31]. The peak load obtained was 4.7 kN, which is slightly less than the peak load of about 5.5kN for W17 CCTS in the current work.

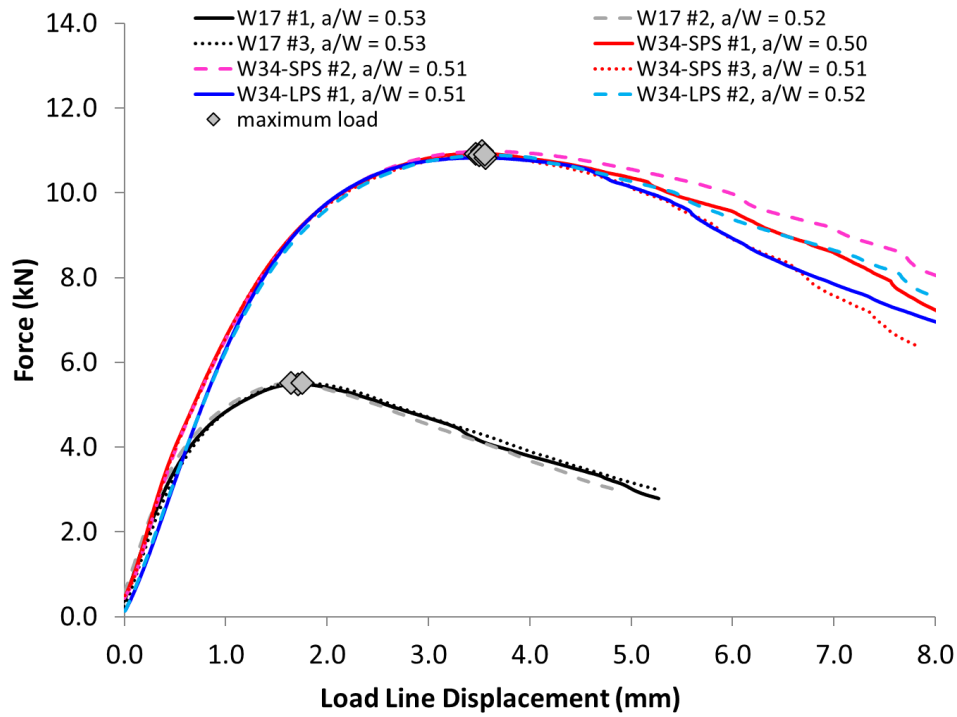**CanmetMATERIALS** ———————————————————————————————

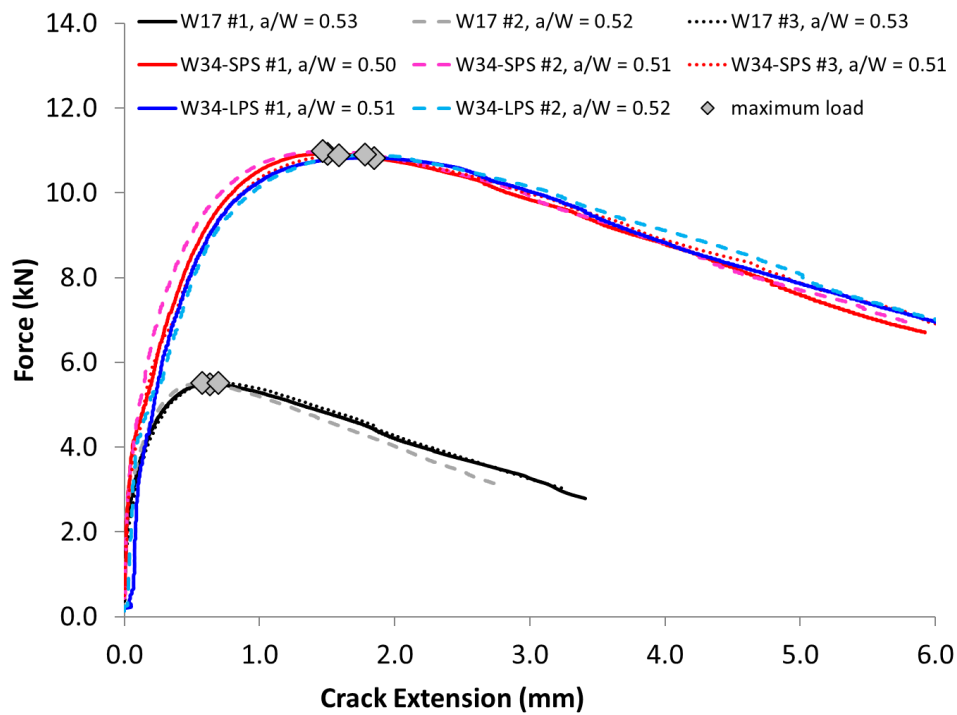Figure 30: Force vs. displacement responses for W17, W34-SPS, and W34-LPS CCTS from Zr-2.5Nb pressure tube material

Figure 31: Force vs. crack extension responses for W17, W34-SPS, and W34-LPS CCTS from Zr-2.5Nb pressure tube material

CanmetMATERIALS

The crack plane and side view images for the W17, W34-SPS, and W34-LPS CCTS are shown in Figure 32, Figure 33, and Figure 34, respectively. Loading pins with a 1° taper were used for all of the tests. ASTM E1820 requires that each of the nine measurements used to calculate crack extension be within $0.05B$ (0.05×4.4 mm $= 0.22$ mm for the current CCTS) of the average crack extension, for both the fatigue precrack and the stable crack growth regimes. For W17 CCTS shown in Figure 32, the differences were all measured to be less than 0.22 mm for the precrack indicating that the tapered pins achieved the requirements in the Standard. As seen in Figure 33a for W34-SPS CCTS, the precrack was reasonably uniform but there was a modest violation of the ASTM requirement. For the W34-LPS CCTS, Figure 34a indicates that a 1° taper was not sufficient to maintain a uniform precrack; a larger-degree taper should be used in future work for this specimen geometry. The side-view images indicate that all of the samples tested underwent flat fracture, with crack tunnelling, and there was no slant fracture. For the stable crack growth regime, there was extensive crack tunnelling which violates the 0.22 mm requirement in the Standard, but this was expected for Zr-2.5Nb as it has been shown that extensive crack tunnelling can occur, particularly in irradiated material as shown in Figure 35 [32].

a)

b)
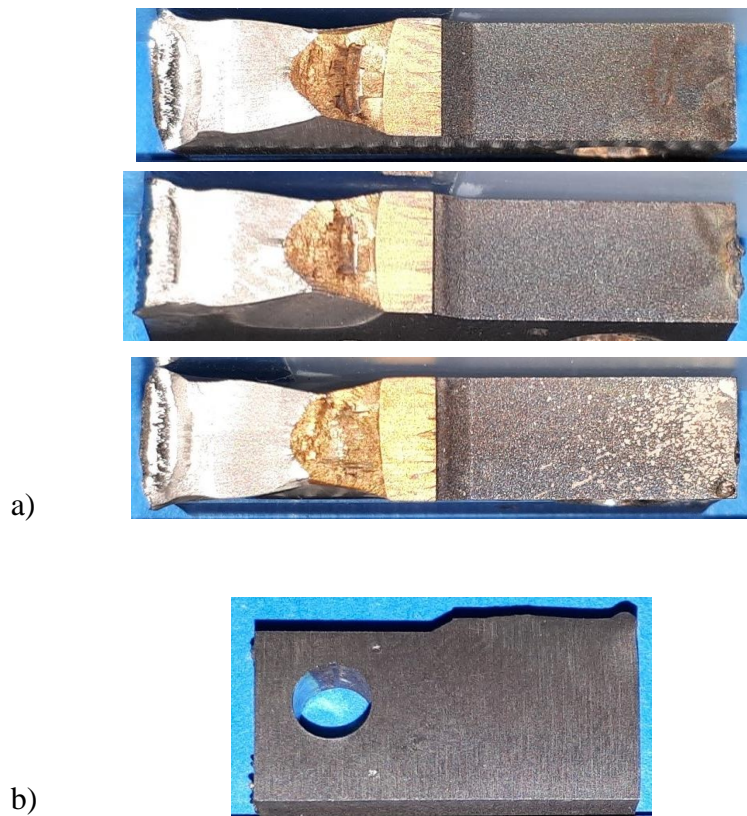
Figure 32: Crack plane and side fracture images of Zr-2.5Nb for W17 CCTS
a) W17 #1, W17 #2, and W17 #3 b) typical side-view

CanmetMATERIALS
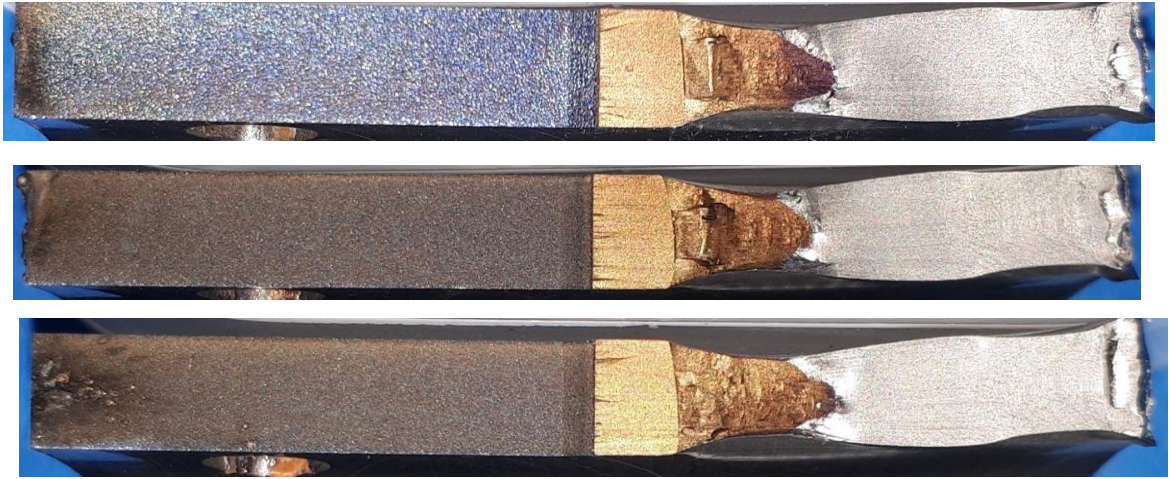
a)

b)

Figure 33: Crack plane and side fracture images of Zr-2.5Nb for W34-SPS CCTS
a) W34-SPS #1, W34-SPS #2, and W34-SPS #3 b) typical side-view

a)

b)

Figure 34: Crack plane and side fracture images of Zr-2.5Nb for W34-LPS CCTS
a) W34-LPS #1 and W34-LPS #2 b) typical side-view

Figure 35: Typical crack tunnelling in Zr-2.5Nb W17 CCTS; fractograph from [32]

5.3 Crack Growth Resistance Curves

The force, displacement, and crack extension data were used to calculate the J-integral using the procedure outlined in ASTM E1820 for a compact tension specimen with a growing crack. The procedure is detailed in Appendix A. The J-integral is plotted versus displacement in Figure 36 and compared between W17, W34-SPS, and W34-LPS CCTS. The figure shows that the maximum load on for W17 CCTS is about half of the maximum load for W34-SPS and W34-LPS CCTS. Up to maximum load, the W34 CCTS results are nearly identical with no noticeable difference in the J-integral versus displacement response between SPS and LPS geometries. After maximum load, there was some deviation in the response for the W34 CCTS geometries.
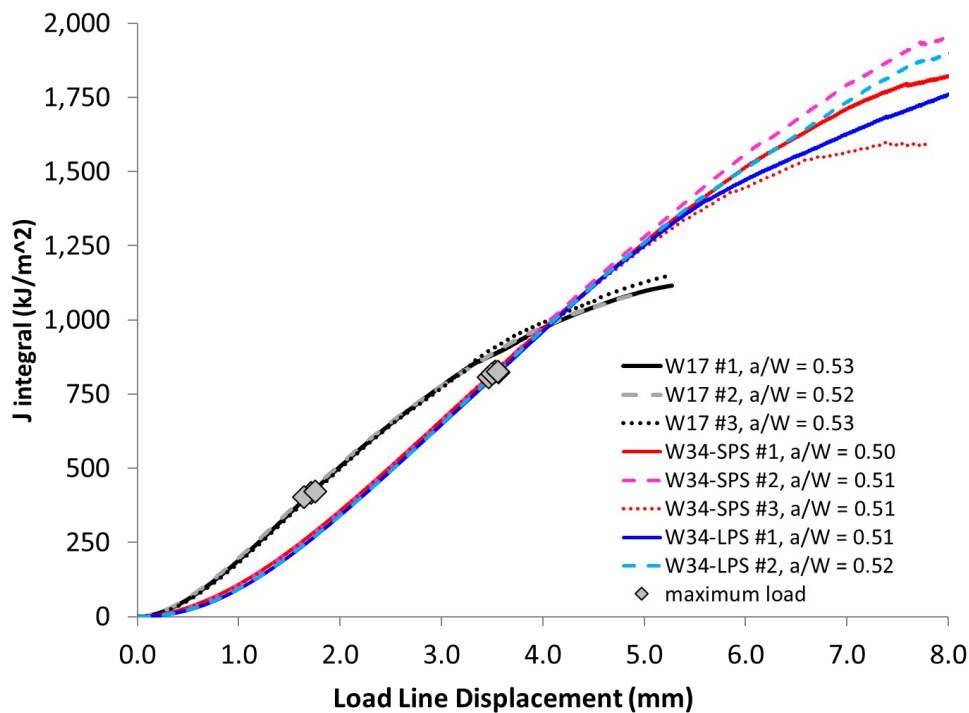

Figure 36: J-integral vs. displacement for W17, W34-SPS, and W34-LPS Zr-2.5Nb CCTS

CanmetMATERIALS _____

The crack growth resistance (J-R) curves are shown in Figure 37 for W17, W34-SPS, and W34-LPS CCTS. Again, the response is consistent between specimens of the same configuration up to maximum load, but begins to deviate after maximum load with larger variation on the W34 CCTS responses at larger values of crack extension. A difference in the initial slope is seen between the W34-SPS and W34-LPS responses.
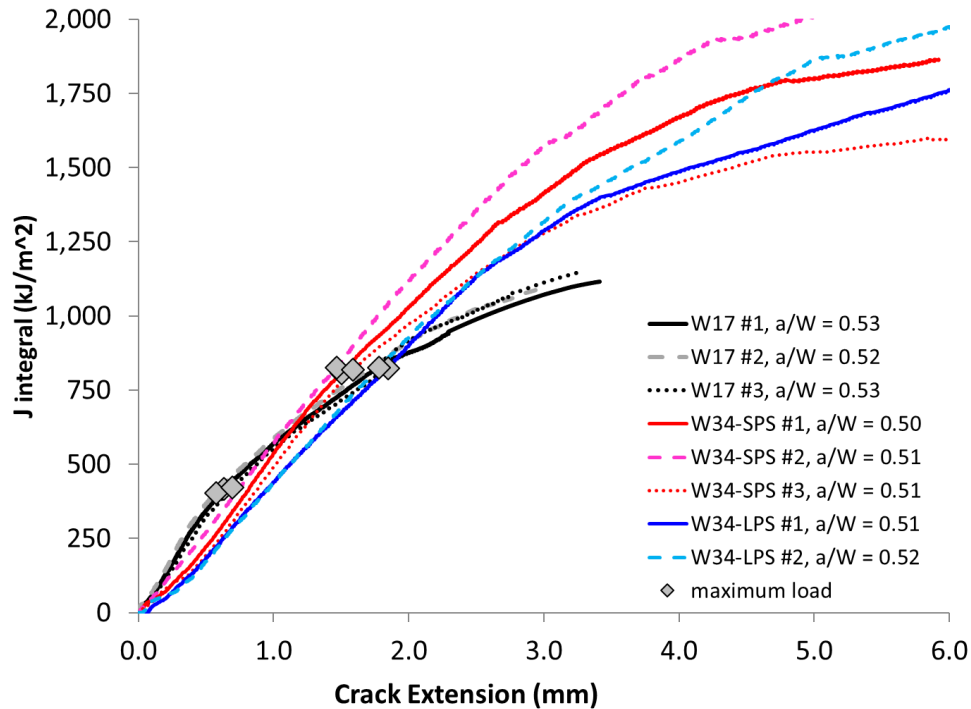
Figure 37: J-integral vs. crack extension for W17, W34-SPS, and W34-LPS Zr-2.5Nb CCTS

The J-values at maximum load, J_{ml}, and the corresponding stress intensity factors at maximum load, K_{ml}, are given in Table 3 with $K_{ml} = \sqrt{J_{ml}E}$ and $E = 102.1$ GPa (which is the Zr-2.5Nb elastic modulus at room temperature). For W17 CCTS, K_{ml} ranged from 202.9 to 207.5 MPa√m. The range for W34-SPS was 287 to 290.5 MPa√m with only a small difference in K_{ml} for the W34-LPS. The average crack extension at maximum load was 0.63 mm for W17 CCTS, 1.5 mm for W34-SPS CCTS, and 1.8 mm for W34-LPS.

Table 3: Fracture Toughness Values at Maximum Load

Test Identification	Maximum Load	Jml	Displacement at Max. Load	Crack Extension at Max. Load	Kml
	kN	kJ/m^2	mm	mm	MPa m^1/2
W17 #1	5.486	416.7	1.71	0.63	206.3
W17 #2	5.508	403.0	1.65	0.57	202.9
W17 #3	5.521	421.8	1.75	0.69	207.5
W34-SPS #1	10.923	806.9	3.46	1.51	287.0
W34-SPS #2	10.983	826.8	3.53	1.47	290.5
W34-SPS#3	10.885	819.7	3.50	1.59	289.3
W34-LPS #1	10.824	823.4	3.56	1.85	290.0
W34-LPS #2	10.902	826.9	3.56	1.78	290.6

When trying to distinguish between the relative benefits of the W34-SPS and W34-LPS test geometries, the results discussed in Section 3 based on a comparison of the J-integrals predicted from finite element simulations of W34-SPS and W34-LPS geometries with a stationary crack should be considered. The predicted ratio of J-values for the two geometries were presented in Figure 14d and Figure 15 and the results indicated a similar response up to a displacement of 0.6 mm. Then, the response began to deviate with a measured difference between J-integral ratio of 20% and 8% at a displacement of 1.0 mm for W34-LPS and W34-SPS, respectively. This indicates that at larger displacement, curvature of the W34-LPS geometry plays a larger, negative role.

The lower bound fracture toughness in the upper shelf regime (above 150 °C) for Zr-2.5Nb pressure tube material with a hydrogen equivalent concentration, $[H_{eq}]$, not exceeding 30 ppm is 72 MPa√m according to CSA N285.8 [41]. The 289 MPa√m average measured for W34-SPS CCTS at room temperature is well above the upper shelf value lower bound value. The fracture toughness of irradiated, hydrided material will be lower than the room temperature as-received response and the transition temperature would be expected to decrease with increased $[H_{eq}]$ due to hydride formation. Hydrided pressure tube material was not considered in the current work to avoid a potential source of variability but could be considered in future work.

6   CONCLUSIONS

The current work studied the fracture toughness of unirradiated Zr-2.5Nb pressure tube material for three different compact tension geometries. The three Curved Compact Tension Specimen (CCTS) geometries were based on a specimen with a width of 17 mm (W17), a width of 34 mm with a small pin-to-pin spacing (W34-SPS) and 34 mm width with a large pin-to-pin spacing (W34-LPS). Finite Element (FE) analyses were performed to assess the applicability of ASTM procedures for computing resistance curves for the three specimen geometries. From the results presented in the preceding sections, it is safe to conclude that the application of the ASTM procedures to the small CCTS over estimates the J-integral and resistance curves by amounts as high as 10%. For the W34-SPS specimen, the resistance curves obtained using the ASTM procedure was in excellent agreement with the resistance curve obtained by averaging the resistance curve (computed from domain integrals) through the thickness of the specimen. FE analyses performed with a stationary crack comparing the W34-SPS and W34-LPS geometry indicate that curvature of the specimen may influence the large-pin-spacing specimen to a greater extent for larger levels of displacement, when compared to the small-pin-spacing geometry.

Mechanical testing was performed on the three CCTS geometries from samples taken from the end of an unirradiated Zr-2.5Nb pressure tube. There were three stages in the curved compact tension test: precracking, stable crack growth, and post-fatigue to failure. It was necessary to use tapered pins to achieve a uniform crack front during the precracking operation on the curved specimen. For W17 and W34-SPS, pins with a 1° taper were sufficient to produce a uniform precrack front. During loading in the stable crack growth regime, it was found that compliance in the load frame and pin bending affect the displacement measurement. A non-contact video extensometer method, as opposed to clip gauges, was used to measure specimen displacement to account for compliance. Consistent J-R curves were calculated for all three CCTS geometries tested from Zr-2.5Nb pressure tube material. Crack initiation occurred significantly before maximum load, so that initiation toughness is considerably less than the maximum load fracture toughness. The stress intensity factors at maximum load for the W17 and W34-SPS CCTS were calculated to be 206 and 289 MPa√m, respectively, an increase of 41% for the wider specimens. The crack extension at maximum load was 0.63 mm for W17 CCTS and 1.5 mm for W34-SPS CCTS, an increase of 140%. The measured fracture responses (J-resistance curves) were similar between W34-SPS and W34-LPS CCTS, but the FE analysis indicated the possible influence of curvature for the W34-LPS geometry at larger levels of displacement and crack extension, beyond the fracture resistance at maximum load considered in the current work. The results in this work are consistent with those presented by Davies et al. [7] for unirradiated Zr-2.5Nb pressure tube material.

_____
CanmetMATERIALS

7   ACKNOWLEDGEMENTS

8   REFERENCES

[1]   Davies P.H., and Shewfelt R.S.W., 1996. Link Between Results of Small-and Large-Scale Toughness Tests on Irradiated Zr-2.5 Nb Pressure Tube Material. In: Zirconium in the nuclear industry, Eleventh International Symposium, ASTM STP 1295, 1295, pp.492–517.

[2]   Simpson L.A., and Chow C.K., 1987. Effect of metallurgical variables and temperature on the fracture toughness of zirconium alloy pressure tubes. In: Zirconium in the nuclear industry, Seventh International Symposium, ASTM STP 939, pp. 579–596.

[3]   Chow, C.K. & Simpson, L.A., 1988. Determination of the fracture toughness of irradiated reactor pressure tubes using curved compact specimens. In Fracture mechanics: eighteenth symposium, ASTM STP 945. pp. 419–439.

[4]   ASTM Standard, 2015. ASTM E1820-15, Standard test method for measurement of fracture toughness.

[5]   Simpson, L.A. & Chow, C.K., 1987. Effect of metallurgical variables and temperature on the fracture toughness of zirconium alloy pressure tubes. In Zirconium in the nuclear industry, Seventh International Symposium, ASTM STP 939. pp. 579–596.

[6]   Ernst, H.A., Paris, P.C. & Landes, J.D., 1981. Estimations on J-integral and tearing modulus T from a single specimen test record. In Fracture mechanics: Thirteenth Conference, ASTM STP 743. ASTM International, pp. 476–502.

[7]   Davies, P.H., Shewfelt, R.S.W. & Järvine, A.K., 1995. Constraint effects in testing different curved geometries of Zr-2.5 Nb pressure tube material. In Constraint Effects in Fracture Theory and Applications: Second Volume, ASTM STP 1244. ASTM International, pp. 393–424.

[8]   Honda, S., 1984. Fracture toughness of Zr-2.5 wt% Nb pressure tubes. Nuclear Engineering and Design, 81(2), pp.159–167.

[9]   Newman Jr, J.C., 1976. Fracture Analysis of Surface and Through Cracks in Cylindrical Pressure Vessels, No. NASA-L-11118, Hampton, VA Langley Research Center.

[10]   Wallace, A.C., 1987. The development of a curved centre cracked specimen for fracture toughness testing of CANDU reactor pressure tubes. MASc. Thesis, Mechanical Engineering Dept., Ottawa University.

[11]   McCabe, D.E. & Ernst, H.A., 1983. A perspective on R-curves and instability theory. In Fracture Mechanics: Fourteenth Symposium—Volume I: Theory and Analysis.

[12]   Landes, J.D., McCabe, D.E. & Ernst, H.A., 1988. Geometry effects on the R-curve. In Nonlinear Fracture Mechanics: Volume II Elastic-Plastic Fracture, ASTM STP 905. ASTM International, pp. 123–143.

[13]   Lucon, E., Scibetta, M., Chaouadi, R., and van Walle, E., 2006. Use of Miniaturized Compact Tension Specimens for Fracture Toughness Measurements in the Upper Shelf Regime. Journal of ASTM International. Vol. 3. pp. 1-16.

[14]   Turner, C.E., 1990. A Re-assessment of Ductile Tearing Resistance. II. Energy Dissipation Rate and Associated R-Curves on Normalised Axes.(Retroactive Coverage). ECF 8: Fracture Behaviour and Design of Materials and Structures., 2, pp.951–968.

[15]   Davies, P.H. & Shewfelt, R.S.W., 1996. Link Between Results of Small-and Large-Scale Toughness Tests on Irradiated Zr-2.5 Nb Pressure Tube Material. Zirconium in the nuclear industry, Eleventh International Symposium, ASTM STP 1295, 1295, pp.492–517.

[16]   Leitch, B. & St Lawrence, S., 2009. Stress-Triaxiality in Zr-2.5 Nb Pressure Tube Materials. In Seventh International ASTM/ ESIS Symposium on Fatigue and Fracture Mechanics (36th ASTM National Symposium on Fatigue and Fracture Mechanics) STP 1508. pp. 540–557.

[17]   Leitch, B.W., 1999. Fracture analyses of an internally pressurized tube containing an axial, through-wall crack. In Fatigue and Fracture Mechanics: 29th Volume. ASTM International.

[18]   Brocks, W. & Scheider, I., 2001. Numerical aspects of the path-dependence of the j-integral in incremental plasticity, GKSS Forschungszentrum, Geesthacht, Germany, Technical Report No.GKSS/WMS/01/08.

[19]   Abaqus6.14, 2014. Abaqus 6.14 documentation. Providence, Rhode Island, USA.

[20]   Shih, C.F., Moran, B. & Nakamura, T., 1986. Energy release rate along a three-dimensional crack front in a thermally stressed body. International Journal of Fracture, 30(2), pp.79–102.

[21]   Moran, B. & Shih, C.F., 1987. A general treatment of crack tip contour integrals. International Journal of fracture, 35(4), pp.295–310.

[22]   Joyce, J.A., 1996. Manual on elastic-plastic fracture: laboratory test procedures, ASTM International.

[23]   Oh, C.-S. et al., 2011. A finite element ductile failure simulation method using stress-modified fracture strain model. Engineering Fracture Mechanics, 78(1), pp.124–137. Available at: http://www.sciencedirect.com/science/article/pii/S0013794410004443.

[24]   Kim, N.-H. et al., 2011. Comparison of fracture strain based ductile failure simulation with experimental results. International Journal of Pressure Vessels and Piping, 88(10), pp.434–447.

[25]   Rice, J.R. & Tracey, D.M., 1969. On the ductile enlargement of voids in triaxial stress fields. Journal of the Mechanics and Physics of Solids, 17(3), pp.201–217.

[26]   Nu-Tech Precision Metals, private communication, April 2017.

[27]   Aitchison, I. & Davies, P.H., 1993. Role of microsegregation in fracture of cold-worked Zr-2.5 Nb pressure tubes. Journal of Nuclear Materials, 203(3), pp.206–220.

[28]   Himbeault D.D., Chow C.K., and Puls M.P., 1994. Deformation behaviour of irradiated Zr-2.5Nb pressure tube material. Metallurgical and Materials Transactions A, Vol. 25A, pp. 135-145.

[29]   ASTM E647-05, "Standard Test Method for Measurement of Fatigue Crack Growth Rates", ASTM Standard, 2005.

[30]   Davies P.H. and Shewfelt R.S.W, 2000. Size, geometry, and material effects in fracture toughness testing of irradiated Zr-2.5Nb pressure tube material. In: Zirconium in the nuclear industry, Twelfth International Symposium, ASTM STP 1354, pp. 356–376.

[31]   Oh S.J., Kim I.S., Kim Y.S., and Ahn S.B., 2005. Fracture toughness of irradiated Zr-2.5Nb CANDU pressure tube using load ratio method. 18th International Conference on Structural Mechanics in Reactor Technology, SMiRT 18.

[32]   Williams B.W., St Lawrence, S. and Leitch B.W. 2011. Comparison of the measured and predicted crack propagation behaviour of Zr-2.5Nb pressure tube material. Engineering Fracture Mechanics, Vol. 78, pp. 3135-3152.

[33]   Rice, J.R., 1968. A Path Independent Integral and the Approximate Analysis of Strain Concentration by Notches and Cracks. Journal of Applied Mechanics, 35(2), p.379.

[34]   Carka, D. & Landis, C.M., 2011. On the path-dependence of the J-integral near a stationary crack in an elastic-plastic material. Journal of Applied Mechanics, 78(1), p.11006.

[35]   Kuang, J.H. & Chen, Y.C., 1996. The values of J-integral within the plastic zone. Engineering Fracture Mechanics, 55(6), pp.869–881. Available at: http://www.sciencedirect.com/science/article/pii/S001379449600077X [Accessed February 16, 2016].

[36]   Hutchinson, J.W., 1989. A course on nonlinear fracture mechanics, Department of Solid Mechanics, Techn. University of Denmark. IAEA-TECDOC-1410, 2002. Delayed hydride cracking in zirconium alloys in pressure tube nuclear reactors.

[37]   Anderson, T.L., 2005. Fracture mechanics: fundamentals and applications, CRC press.

_____ **CanmetMATERIALS**

[38]   Joyce, J.A. & Link, R.E., 1995. Effects of constraint on upper shelf fracture toughness. In
         Fracture Mechanics: 26th Volume. ASTM International.

[39]   Xia, L., Shih, C.F. & Hutchinson, J.W., 1995. A computational approach to ductile crack
         growth under large scale yielding conditions. Journal of the Mechanics and Physics of
         Solids, 43(3), pp.389–413.

[40]   Zhu, X.-K. & Joyce, J.A., 2012. Review of fracture toughness (G, K, J, CTOD, CTOA)
         testing and standardization. Engineering Fracture Mechanics, 85, pp.1–46.

[41]   CSA N285.8-05, 2005. "Technical requirements for in-service evaluation of zirconium
         alloy pressure tubes in CANDU reactors", The Canadian Standards Association.

APPENDIX A: J-INTEGRAL

The J-integral represents an energy release rate. It is a contour integral that may be evaluated around cracks and notches. In practice, the value of the J-integral is used to evaluate fracture toughness. Under conditions of non-linear elastic material response under Mode I loading with small-scale yielding, the J-integral evaluated around a stationary crack has been demonstrated to be path independent, Rice [33].   However, Carka & Landis [34] have shown that in an elastic-plastic material, the J-integral is not path independent, particularly if the contour around which the integral is evaluated approaches the crack tip. The J-integral is also path dependent for non-proportional loading or for steadily growing cracks, the latter being due to non-proportional loading that prevails at the crack tips. In this regard, Kuang & Chen [35] carried out finite element analyses of a C(T) geometry with an elastic-plastic material model and showed that unless the contour used to evaluate the J-integral was sufficiently far away from the plastic zone around the crack tip, path dependence was observed.

Further complications arise when the crack grows. The resistance curve (R-curve), which describes the dependence of the J-integral on crack growth, is an important characteristic and may be used to evaluate structural stability. In evaluating J-integrals for growing cracks, the remaining ligament size must be large enough to ensure stable J-dominated growth. For a discussion of these points, the monograph by Hutchinson [36] or the text by Anderson [37] may be consulted. Alternatives such as Crack-Tip Opening Displacement or Crack-Tip Opening Angle are available but not within the scope of the present project.

Additionally, under large-scale yielding conditions for growing cracks, experimental resistance curves for steel have been shown to be constraint (or geometry) dependent, Joyce & Link [38]. Owing to the geometry of the sample, elastic material surrounding the crack constrains plastic flow and this in turn impacts the resistance to crack growth. Though the resistance curves are only marginally different at initiation and low crack extensions, when sufficient (typically > 1 mm) crack growth has occurred, the resistance curves depend on specimen geometry. These experimental observations have been reproduced in the computational work carried out by Xia et al. [39] who used the computational cell approach and the Gurson-Tvergaard-Needleman failure criteria to model crack growth.

In essence, to obtain J-integrals, the load on the specimen, the displacement of the load point, and the magnitude of crack growth (if the crack grows) are required. Significant effort has gone into the methodology for calculation of J from test data for various geometries, and for a recent review the article by Zhu & Joyce [40] may be consulted. Therein the evolution of J-integral evaluation procedures is discussed. In particular, the J-integral is specimen-dependent for conventional engineering materials and typical applications; that is, the R-curve is not a material property but depends also on the geometry, for example the loading mode and specimen size.

Provided that the test specimen geometry replicates the stress state of the structure whose integrity is being assessed, the J-integral or R-curve provides a powerful way of describing the fracture toughness. An alternative approach would be to measure the displacement fields around the crack tip and evaluate the fracture toughness directly using an appropriate material model; this approach is much more cumbersome and complex.

_____ **CanmetMATERIALS**

In practice, to incorporate a margin of safety the J-integral or R-curve (i.e. the fracture toughness) may be evaluated under plane-strain conditions, which represent limiting conditions and provide an asymptote (conservative bound) to the material property. Accordingly, the ASTM E1820 procedures have been developed to measure the elastic-plastic initiation toughness J_{IC} and $J - R$ curves for specimens that impose high crack-tip constraint and provide conservative estimates of fracture toughness.

The following equations pertain to stationary C(T) crack evaluation. With knowledge of the load-displacement record, the elastic crack driving force is evaluated using

$$K = \frac{P}{B\sqrt{W}} f\left(\frac{a}{W}\right),$$

(A-1)

where K is the stress intensity factor, P the load, W the specimen width, B the specimen thickness, and f an empirical function of a/W. The function f, specific to the C(T) specimen, is given by

$$f\left(\frac{a}{W}\right) = \frac{2 + \frac{a}{W}}{\left(1 - \frac{a}{W}\right)^{3/2}} \left[0.886 + 4.64\left(\frac{a}{W}\right) - 13.32\left(\frac{a}{W}\right)^2 + 14.72\left(\frac{a}{W}\right)^3 \right. $$
$$\left. - 5.6\left(\frac{a}{W}\right)^4\right].$$

(A-2)

The elastic part of the J-integral is given by

$$J_e = \frac{K^2(1 - \nu^2)}{E},$$

(A-3)

where E and ν are Young's modulus and Poisson's ratio, respectively, and K is given by Eq. (A-1). To compute the plastic part of the J-integral, the area under the load-plastic displacement curve A_{pl} is computed (see Fig. A1.3 in Annex A of ASTM E1820) and then used in

$$J_{pl} = \frac{\eta A_{pl}}{B(W - a)},$$

(A-4)

where $\eta = 2 + 0.522 (W - a)/W$ and it is a geometry-specific empirical factor. The total J-integral is given by

$$J = J_e + J_{pl}$$

(A-5)

In the case of a growing crack, the total J-integral is given by

CanmetMATERIALS _____

$$J = \frac{K_{(i)}^2(1 - v^2)}{E} + J_{pl(i)}, \tag{A-6}$$

where the subscript in parentheses (i) indicates that the evaluation is for the current crack length $a_{(i)}$.

The plastic part of the J-integral for the current crack length crack reads

$$J_{pl(i)} = \left[J_{pl(i-i)} + \left(\frac{\eta_{(i-1)}}{b_{(i-1)}} \right) \frac{A_{pl(i)} - A_{pl(i-1)}}{B} \right] \left[1 - \gamma_{(i-1)} \frac{a_{(i)} - a_{(i-1)}}{b_{(i-1)}} \right]. \tag{A-7}$$

In the above equation, $A_{pl(i)} - A_{pl(i-1)}$ represents the area under the force versus plastic displacement record for the increment of crack growth $a_{(i)}$-$a_{(i-1)}$ and its evaluation is elaborated upon in Fig. A1.3 in Annex A1 of ASTM E1820.

APPENDIX B: ASTM E08 MEETING

The results of the work presented in this report were presented at the ASTM E08.07.05 (Ductile Fracture) meeting held in San Diego in May 2018. This appendix captures the discussion held during the meeting. Below are comments and discussion resulting from the presentation.

- It was stated in the presentation that "The *J*-integral predicted from simulations ranged between ± 5 - 13 % of *J*-values from E1820".
  - o It was suggested that the results of the simulations should be presented in a table to distinguish the percent different between geometry curvature, crack front curvature, and specimen size deviations from ASTM standard.
  - o It was questioned whether the stationary crack growth simulations were based on simulation at *a/W* = 0.5 or *a/W* = 0.7 (at end of test). In other words, does the *a/W* ratio affect the prediction ?
  - o There was some discussion as to whether 5-13% is a significant difference and it was mentioned that this variation is relative to entire dataset (for which there is considerable variation for Zr-2.5Nb).

- Images of crack front curvature for irradiated and unirradiated Zr-2.5Nb CCTS W17 specimens were shown in the presentation.
  - o It was discussed that the tunnelling behaviour observed in (irradiated) Zr-2.5Nb is the opposite of what is seen in other metallic alloys (e.g. steel, aluminum).
  - o Zr-2.5Nb demonstrates extensive tunnelling for the irradiated (lower toughness) with a lower amount of tunnelling for the unirradiated material (high toughness); there was a question as to whether the irradiation damage is constant through the thickness (if not, this could lead to extensive tunnelling).

- It was highlighted in the presentation that the W34 – geometry with a lower pin spacing of 0.167W was different than recommended in E1820 (0.355W for J-integral and 0.275W for K1c testing); this received no comments.

- Also, there were no comments related to the high *W/b* ratio for the W34 – low pin spacing geometry, although this was highlighted in the presentation.
  - o W/b = 34 mm / 4.4 mm = 7.7 → no comments
  - o W/b = 17 mm / 4.4 mm = 3.9

- There was a general comment as to why an axial crack is considered.

- There was a comment related to irradiated testing, as to whether bulging during a burst test affects subsequent properties of the pressure tube from which CCTS and transverse tensile specimens are machined and tested.

CanmetMATERIALS _____

Additional comments recorded during the ASTM E08.07.05 (Ductile Fracture) session are identified below.

- Prior to the Zr-2.5Nb presentation, Professor Dodds gave a presentation on the influence of crack front curvature on the J-integral. It was highlighted that a 3% variation in J-integral due to typical crack front curvature might be expected; the level of crack front curvature was not captured. It is anticipated that this will be included in an Appendix of E1820 (to be voted on in future). The level of tunnelling did not appear to be as extensive as with (irradiated) Zr-2.5Nb. However, the effect on the J-integral predicted in growing crack simulations performed for Zr-2.5Nb in the current work to simulate the influence of tunnelling were in reasonable agreement with the results presented by Professor Dodds.

- There was some discussion as to the use of side grooves to prevent tunnelling. It was made clear that for Zr-2.5Nb side grooves were not considered for CCTS as the crack also tunnels in the rising pressure burst tests and the objective is to generates resistance curves applicable to the pressure tube geometry.

- There was some discussion as to whether the 'time' needed to be calibrated on loading frames. This is in addition to recording load cell and LVDT measurements.

- E1820 will be proceeding with an appendix for DCPD. Comments provided by Dr. Bill Tyson about crack tip blunting were discussed.

- A presentation on the multi-specimen J-R curve approach was moved to the next ASTM meeting.

- There are plans to re-write E1820 to reduce the size of the standard (e.g. to reduce the many appendices in the standard).

- The close relationship between E1820 and E1921 (Standard Test Method for Determination of Reference Temperature, To, for Ferritic Steels in the Transition Range) was evident. There was discussion about voting on an Ω factor in E1921.

APPENDIX C: TOOLING SCHEMATICS

In this appendix, detail drawings of the gripping mechanisms for the W17, W34-SPS, and W34-LPS CCTS are provided. The grips were designed to incorporate pins of diameter 4.2 mm, 5 mm, and 8.5 mm for the W17, W34-SPS, and W34-LPS CCTS, respectively. The actual diameter of the tapered pins used in the testing was slightly smaller than these diameters to accommodate the thickness of electrical isolation applied to the pins. During fracture testing of the W34-SPS CCTS, it was found that the 5 mm pin could bend under the load of the unirradiated Zr-2.5Nb pressure tube samples tested at room temperature. Future work could consider using larger diameter pins to prevent bending for W34-SPS CCTS, but the grip design would need to be modified slightly to accommodate the larger pin, yet ensure that the area of the grip subject to contact with the pin can withstand the applied loading.
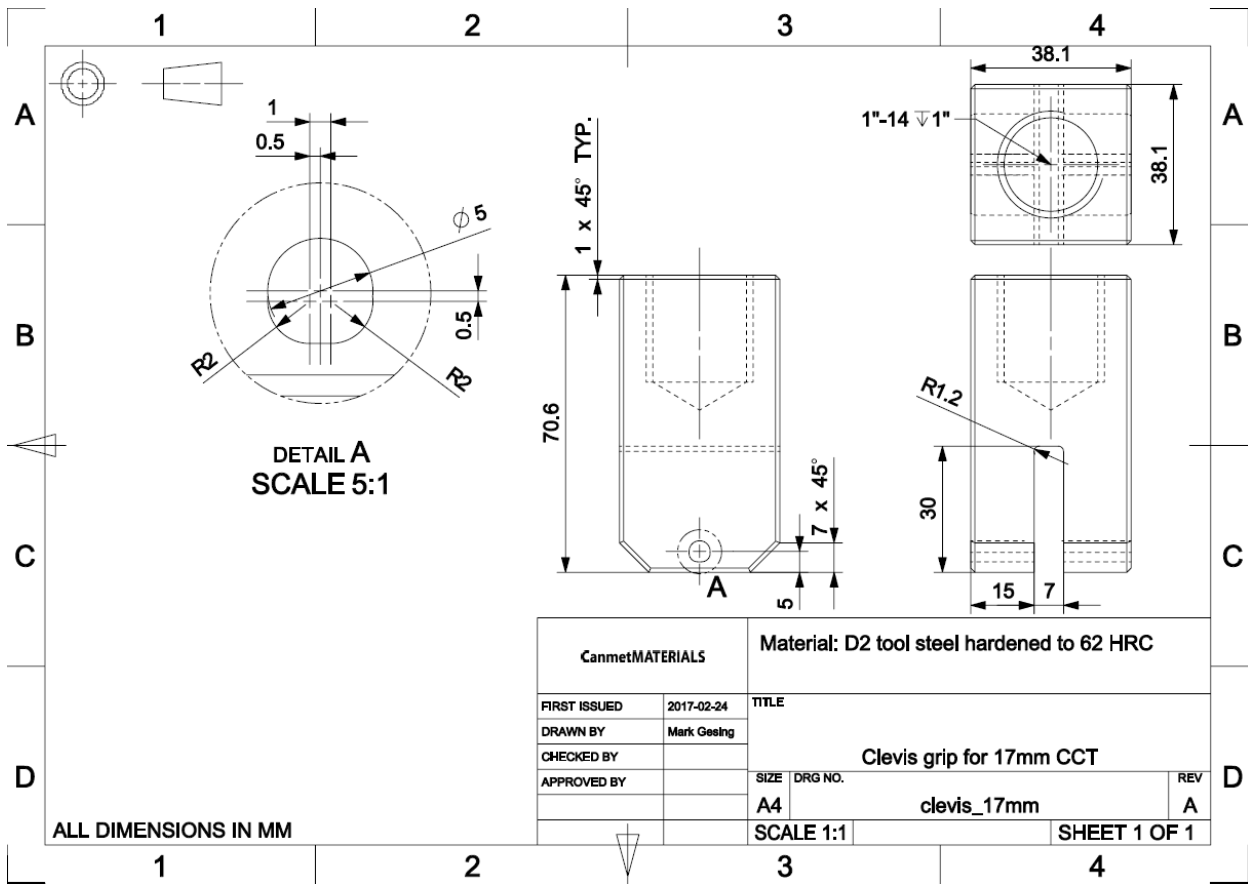

Figure A-1: Grip geometry for W17 CCTS geometry

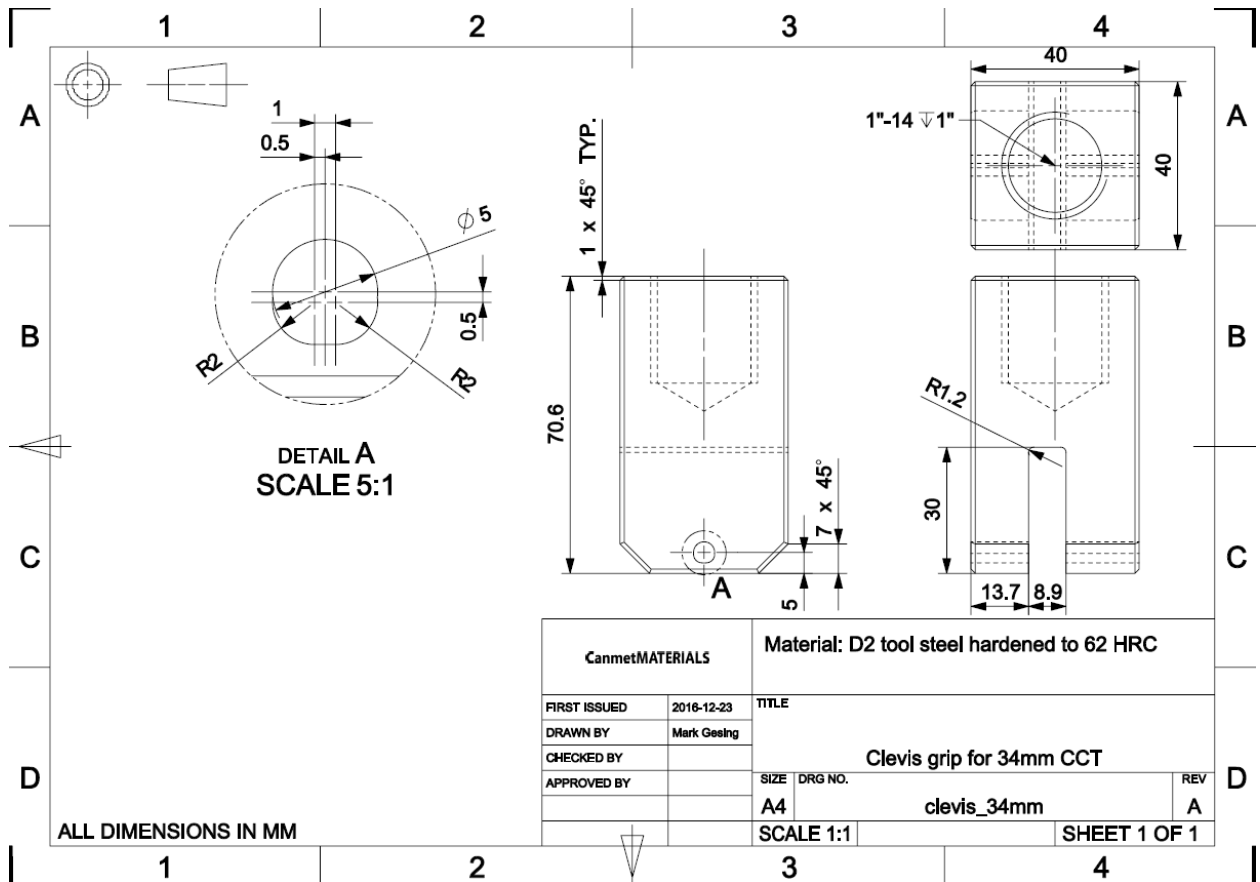**CanmetMATERIALS** ——————————————————————————————————————
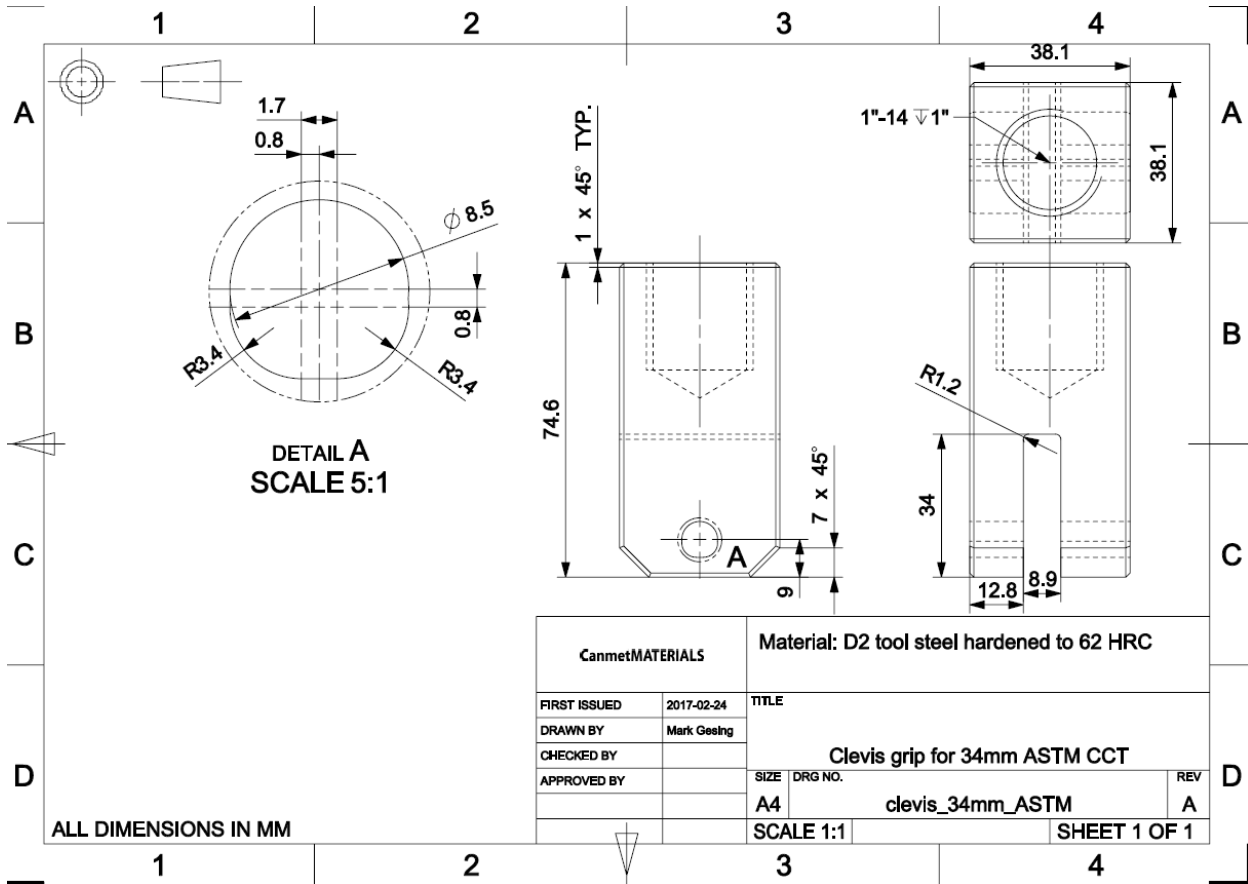
Figure A-2: Grip geometry for W34-SPS CCTS geometry

Figure A-3: Grip geometry for W34-LPSCCTS geometry